HER2-driven mammary tumorigenesis enhances bioenergetics despite reductions in mitochondrial content

Sara M Frangos[1], Henver S Brunetta[1], Dongdong Wang[2,3], Maria Joy Therese Jabile[2,3], Leslie Jeffries[4], Grace Mencfeld[4], David W L Ma[1], William J Muller[5], Cezar M Khursigara[6], Kelsey H Fisher-Wellman[7], Jim Petrik[4], Gregory R Steinberg[2,3], Graham P Holloway[1]

[1]Department of Human Health Sciences, University of Guelph, ON, Canada
[2]Centre for Metabolism, Obesity and Diabetes Research, McMaster University, Hamilton, ON, Canada
[3]Division of Endocrinology and Metabolism, Department of Medicine, McMaster University, Hamilton, ON, Canada
[4]Department of Biomedical Sciences, University of Guelph, ON, Canada
[5]Department of Biochemistry, McGill University, Rosalind and Morris Goodman Cancer Research, Montreal, QC, Canada
[6]Department of Molecular and Cellular Biology, University of Guelph, ON, Canada
[7]Department of Cancer Biology, Medical Center Boulevard, Wake Forest University School of Medicine, Winston-Salem, NC, USA
Corresponding authors: Sara M Frangos (sfrangos@uoguelph.ca) and Graham P Holloway (ghollowa@uoguelph.ca)

ABSTRACT

It is now recognized that mitochondria play a crucial role in tumorigenesis, however, it has become clear that tumor metabolism varies significantly between cancer types. The failure of recent clinical trials aimed at directly targeting tumor respiration through oxidative phosphorylation inhibitors underscores the critical need for further studies providing an in-depth evaluation of mitochondrial bioenergetics. Accordingly, we comprehensively assessed the bulk tumor and mitochondrial metabolic phenotype in murine HER2-driven mammary cancer tumors and benign mammary tissue. Transcriptomic and proteomic profiling revealed a broad downregulation of mitochondrial genes/proteins in tumors, including OXPHOS subunits comprising Complexes I-IV. Despite reductions in tumor mitochondrial proteins, mitochondrial respiration was several-fold higher compared to benign mammary tissue, which persisted regardless of normalization method (wet weight, total protein content and when corrected for mitochondrial content). This upregulated respiratory capacity could not be explained by OXPHOS uncoupling, suggesting HER2 signaling regulates intrinsic mitochondrial bioenergetics. In further support, lapatinib, an EGFR/HER2 tyrosine kinase inhibitor, attenuated mitochondrial respiration in NF639 murine mammary tumor epithelial cells. Together, this data highlights that the typical correlation between mitochondrial content and respiratory capacity may not apply to all tumor types and implicates HER2-linked activation of mitochondrial respiration supporting tumorigenesis in this model.

INTRODUCTION

The field of cancer metabolism has rapidly evolved in the last decade. A specific focus of many researchers has been on understanding the role of mitochondria in tumorigenesis with the goal to potentially target aspects of mitochondrial metabolism to reduce proliferation[1,2]. It was initially hypothesized that a universal characteristic of cancer cells was dysfunctional oxidative phosphorylation (OXPHOS), as proposed by Otto Warburg in the 1920s[3,4]. This theory spurred interest in studying mitochondria in various cancers, highlighting the diverse mitochondrial phenotypes in this context. While instrumental for OXPHOS, mitochondria are now recognized for their multifaceted roles in regulating cellular homeostasis, including supporting macromolecule biosynthesis[5], maintaining redox balance[6] and generating metabolites that regulate gene transcription[7]. Given their pleiotropic effects within the cell, there is growing recognition that mitochondria play an essential role in cancer initiation, progression, and metastasis[1], and an appreciation that interrogating mitochondrial bioenergetics in diverse cancers may identify novel therapeutic strategies.

Reductions in the content/activity of mitochondrial enzymes within the tricarboxylic acid (TCA) cycle and electron transport chain (ETC) often correlate with impaired mitochondrial respiratory capacity and coincides with activating transcriptional programs driving tumorigenesis[8–10]. Indeed, inhibition of succinate dehydrogenase (Complex II) in osteosarcoma cells[8], and renal cell carcinoma[9] enhances cancer growth despite OXPHOS inhibition. Furthermore, in colorectal cancer, age-related Complex I deficiency coincides with reduced respiratory capacity but enhanced serine synthesis and subsequent growth rates[10]. Despite this evidence suggesting that disruptions in mitochondrial bioenergetics contribute to tumor progression, several elegant studies using genetic and pharmacological approaches have solidified that a functional ETC is required for cancer cell growth [6,11,12]. Furthermore, the use of whole-genome sequencing specifically interrogating mtDNA phenotypes across several human cancers has revealed that loss of function mutations in mtDNA genes are often under negative selection[13], suggesting the maintenance of mitochondrial function may support tumorigenesis in some cancers and impairments in mitochondrial metabolism are not a ubiquitous finding. However, mitochondrial content represents one dimension of bioenergetic regulation and does not alone determine respiratory capacity. Therefore, a comprehensive assessment of mitochondrial function, particularly within the context of the mitochondrial proteome, is warranted to provide deeper insights into the relationship between mitochondrial content and bioenergetics in different cancers.

Within this framework, there has been considerable interest in investigating mitochondrial bioenergetics and dynamics in breast cancer subtypes due to the limited therapeutic options for triple-negative breast cancer (TNBC) and therapeutic resistance in breast cancers driven by estrogen (ER), progesterone (PR) and human epidermal growth factor (HER2) receptor amplification[14–16]. Indeed, increases in mitochondrial respiration or "OXPHOS reliance" is associated with poor outcomes in treatment naïve TNBC[17], metastatic ER+ tumors[18], and HER2-driven breast cancers[19]. While inhibiting OXPHOS in this context[17,18] (i.e. with Complex I inhibitor IACS-010759) has shown some pre-clinical success, systemic toxicity has prevented the translation of this strategy to the clinic[20]. Furthermore, it is unclear whether increases in mitochondrial respiration arise from increases in mitochondrial content or intrinsic enhancements in mitochondrial function (e.g. coupling efficiency, substrate delivery/sensitivity, oncogenic signaling events). This information is critical to develop successful mitochondrial-targeted therapies with a wider therapeutic window. Thus, in the current study, we comprehensively assessed the bulk tumor and mitochondrial phenotype between murine HER2-driven mammary cancer tumors and benign mammary tissue in the context of the underlying transcriptome and proteome. Respiratory capacity supported by both pyruvate and lipids was enhanced in HER2-driven tumors despite lower mitochondrial content compared to benign mammary tissue. Mitochondrial bioenergetics were supressed by the dual tyrosine kinase inhibitor lapatinib, suggesting events linked to HER2-mediated oncogenic signaling may drive increases in OXPHOS during tumorigenesis.

RESULTS

Mammary tumors from MMTV/neu^{ndl}-YD5 mice display canonical HER2 pathway activation

Cell lines are commonly used to study isolated mechanisms driving tumorigenesis, however, they neglect the variety of cell types in the tissue of origin and the influence of the tumor microenvironment, which is a key regulator of cancer growth[21,22]. To this end, we have utilized tumor and benign mammary tissues from MMTV/neu^{ndl}-YD5 transgenic mice[23] to investigate HER2-driven tumor biology **(Fig.1A).** Signaling events linked to HER2 activation rely on the autophosphorylation of the tyrosine kinase domain[23–25] and MMTV/neu^{ndl}-YD5 mice possess an add-back mutation at the Y1226/7 (YD) site, activating downstream signaling events linked to SHC/GRB2 with similar transforming potential as the wild-type protein[25,26] **(Fig.1B)**. While the proximal signaling events linked to HER2 activation in this model have been described[25], to validate our bulk tissue-based model, we assessed the mRNA (transcriptomics) and protein (quantitative label-free proteomics and western blotting) expression of canonical HER2 pathway members (RAS/MAPK and PI3K/AKT/mTOR pathways) that are well-characterized in various HER2-overexpressing mammary cancer cell lines **(Fig.1B)**[27–29]. *Her2* transcript levels were increased ~175-fold (**Fig.1C**) and transcripts belonging to the Ras/MAPK (*Hras, Mapk1, Mapk3*) and PI3K/AKT/mTOR (*Pik3cg, Pik3c2a,*

Pik3c2b, Pikrcg, Pik3c3, Akt3) pathways were also upregulated in the tumors compared to the benign mammary tissue **(Fig.1D)**. At the protein level, HER2 was readily detectable in mammary tumors by quantitative label-free proteomics but undetectable in paired benign tissues **(Fig.1E)** suggesting enhanced HER2 transcription also manifests as an increase in receptor content in the tumors. Downstream of HER2 activation, the total protein content of p38 MAPK, ERK1/2 and eEF2 were significantly increased in tumors compared to benign tissue detected by western blot **(Fig.1F,G)**. When normalized to total protein, p38 MAPK and eEF2 phosphorylation were not higher in tumors due to proportional increases in total protein abundance, while in contrast, phosphorylated ERK1/2 and mTOR were significantly upregulated suggesting both Ras/MAPK and the PI3k/AKT/mTOR pathways were activated in tumors **(Fig.1H, S-Fig.1)**. Overall, these data demonstrate that mammary tumors display classical hallmarks of HER2-driven cancer cell signaling, allowing for the subsequent investigation of HER2-driven tumor biology and metabolism in this model.

Assessment of the HER2-driven mammary tumor transcriptome

To understand the biology and metabolism of HER2-driven mammary tumors, we assessed their transcriptomes using RNA sequencing. Principal component analysis (PCA) using the entire gene expression profile showed distinct separation between groups **(Fig.2A)**. Visualizing all differentially expressed genes (DEGs) using a volcano plot **(Fig.2B)** and the top 3000 DEGs using a heatmap **(Fig.2C)** revealed several differentially upregulated and downregulated genes between groups where genes involved in MAPK- and AKT-linked signaling, ECM remodelling and cellular stress responses *(Etv1, Dusp6, Papln, Ier3*) were among the most upregulated genes in the tumors and genes involved in lipid metabolism (*Dgat2, Lipe, Cd36*) were among the most downregulated. Enrichment analysis of the top 3000 upregulated DEGs **(Fig.2D)** identified pathways characteristic of HER2-driven signaling (e.g. tyrosine kinase signaling, GTPase signaling) and gene ontology (GO) analysis identified processes indicative of active transcription, translation, and protein turnover characteristic of a rapidly proliferating tissue **(Fig.2E)**. Interestingly, enrichment analysis of the top 3000 downregulated genes in the tumors consistently identified that mitochondrial metabolism, and in particular components of the oxidative phosphorylation (OXPHOS) system, were downregulated in tumors compared to benign mammary tissue **(Fig.2F,G)**.

Assessment of HER2-driven mammary tumor proteome

We further validated our bulk-tissue transcriptomic findings at the protein level using label-free quantitative proteomics and detected 2589 proteins in the benign mammary tissue and 2448 proteins in the HER2-driven tumors; 1848 of which were found in both groups **(Fig.3A)**. This initial analysis revealed 741 and 600 uniquely expressed (i.e. only detected in one tissue) proteins in benign mammary tissue and tumors respectively **(S-Fig.2A)**. Interestingly, OXPHOS and aerobic respiration were identified among the top pathways in benign tissue, but not in tumors **(S-Fig.2B-G)**, further supporting the notion of downregulated mitochondrial content within tumors. Reflecting the PCA for the transcriptomic data, analysis of all overlapping proteins between benign and tumor samples revealed distinct separation **(Fig.3B)**. Of the 1848 proteins found in both the tumors and benign tissue, 420 were significantly different (p-adj. <0.1, **Fig 3A,C,D**). However, the majority of the differentially expressed proteins were downregulated (n=411) in tumors compared to benign mammary tissue. Upregulated proteins (n=9) included those involved in canonical HER2 signaling, protein synthesis and processing, and glycolytic metabolism **(S-Table 1)**. Supporting transcriptomic data, which indicated a reduction in mitochondrial content and OXPHOS, enrichment analysis revealed that 8 of the top 10 downregulated pathways **(Fig. 3E)** and all top 10 downregulated GO **(Fig. 3F)** were related to mitochondrial biogenesis and/or metabolism, and OXPHOS was identified in the top 10 downregulated KEGG pathways **(Fig.3G)**. Together, these proteomic data support our transcriptomic analysis suggesting HER2-driven tumors are characterized by lower mitochondrial content than benign mammary tissue.

Integrated assessment of the HER2-driven tumor transcriptome and proteome

The concordant nature of our transcriptomic and proteomic datasets was highlighted when correlating the log2FC between overlapping gene and protein targets **(Fig.4A)**. Sorting these data by mitochondrial

proteins highlighted that the majority of overlapping mitochondrial proteins detected in both datasets were downregulated **(Fig.4B)**. Thus, we further analyzed the 144 overlapping downregulated targets between these analyses **(Fig.4C)**. KEGG enrichment analysis of the downregulated targets identified OXPHOS among the top 10 pathways, as well as carbon metabolism, BCAA degradation and fatty acid metabolism which encompass numerous mitochondrial targets **(Fig.4D)**. The top 10 common downregulated pathways **(Fig.4E)** and GO **(Fig.4F)** all pertained to mitochondrial substrate metabolism/catabolism and OXPHOS. Together, transcriptomic and proteomic analyses strongly support that HER2-driven tumors are characterized by downregulated mitochondrial content.

Assessment of the mitochondrial transcriptome and proteome

Our initial transcriptomic and proteomic analyses encompassed all differentially expressed genes/proteins between tissues (including mitochondrial targets) and clearly identified reductions in mitochondrial content in the tumors. This emphasized the robust nature of mitochondrial adaptations in this model, considering mitochondrial proteins (identified using the mouse MitoCarta 3.0 database) represented a small fraction of total cellular protein in both tumors and benign mammary tissue **(S-Fig.3A)**. By filtering our proteomic dataset using MitoCarta, we identified 125 mitochondrial proteins that were commonly expressed between the tumors and benign mammary tissue **(Fig.5A)**. When visualizing the 125 proteins with a heatmap, the majority of the mitochondrial proteome was downregulated in the tumors compared to the benign mammary tissue **(Fig.5B)**. The summed absolute abundance of all detected mitochondrial proteins in each group was also lower in tumors **(Fig.5C)**, again supporting our transcriptomic and proteomic analyses suggesting a reduction in mitochondrial content exists in the tumors.

While mitochondrial biogenesis is a coordinated process simultaneously upregulating several mitochondrial proteins, the total mitochondrial transcriptome/proteome does not necessarily change proportionally with OXPHOS complex and/or TCA cycle/dehydrogenase content, especially in cancerous tissues. Indeed, reductions in the content of certain respiratory complexes seem to be cancer specific, which can have functional repercussions on mitochondrial respiration rates and/or efficiency[10,31]. Within this context, we assessed the gene expression profile of all OXPHOS complex subunits between groups, which revealed relatively ubiquitous reductions in transcript count (transcripts per million) across subunits of Complexes I-IV in the tumors **(Fig.5D-H)**. Interestingly, while the majority of Complex V subunits were also downregulated, this complex had the highest proportion of subunits displaying no differences between groups **(Fig.5D,I)**. The TCA cycle transcriptome also reflected a general downregulation of transcript abundance, apart from alpha-ketoglutarate dehydrogenase (*Ogdhl*) and succinyl-CoA synthetase GDP forming subunit-β (*Suclg2*), which had a higher transcript abundance in some tumor samples **(Fig.5J)**. While we focused on transcriptomic data for this analysis due to lower detection of certain OXPHOS subunits using label-free quantitative proteomics **(S-Fig.4A-E)**, the summed abundance of all OXPHOS subunits detected per complex expressed relative to the underlying mitochondrial proteome **(S-Fig.4F),** and relative to the total proteome **(S-Fig.4G)** displayed a similar pattern. This interpretation was further validated by western blot, where tumor CII and CIV content were lower than benign mammary tissue **(S-Fig.4H).** Overall, these data further suggest that the mitochondrial proteome and OXPHOS Complexes I-IV are downregulated in HER2-driven tumors.

While these findings strongly support reduced mitochondrial gene expression in tumors, differences could theoretically result from shifts in cell-type during tumorigenesis. To address this, we first assessed OXPHOS expression in a publicly available single-cell RNA sequencing (scRNA-seq) dataset from human breast tumors[31]. In the scRNA-seq dataset, tumor epithelial cells expressed the highest proportion of CI-CIV subunits when grouped by cell type **(Fig.6A,B).** We next assessed cell-type composition in our tumor and benign mammary tissue samples by immunofluorescence **(Fig.6C)**. Although the immunopositive area was lower across all cell types in benign samples**,** mesenchymal and epithelial cells remained the dominant populations in both groups, indicating the absence of major shifts in the most abundant cell types **(Fig.6D).** To integrate cell-type-specific OXPHOS mRNA expression (scRNA-seq) with cell-type abundance in our samples, we calculated a cell-type-weighted OXPHOS mRNA Index, reflecting each population's estimated contribution to Complex I–V transcript levels in our tissues. The OXPHOS mRNA Index **(Fig.6E)** indicated

198 that epithelial cells were likely the dominant contributors to OXPHOS transcripts in the present tumor
199 samples. When these values were summed across complexes to generate a Total OXPHOS mRNA Score,
200 epithelial cells remained the primary contributors **(Fig.6F).** Altogether, these analyses suggest that our
201 whole-tissue RNA-seq signatures are consistent with canonical HER2-driven signaling and indicate that the
202 reduction in OXPHOS gene expression observed by bulk-tissue RNA-seq likely cannot be explained by a
203 loss of high-OXPHOS epithelial cells or a gain in low-OXPHOS cell populations. Instead, these findings
204 support a cell-intrinsic suppression of mitochondrial gene expression in HER2-driven tumors.

205 **Mitochondrial respiratory capacity is increased in HER2-driven mammary tumors**

206 Considering our transcriptomic and proteomic data strongly suggest HER2-driven mammary tumors
207 display reductions in mitochondrial content, we next assessed whether this would manifest as a reduction
208 in respiratory capacity by measuring mitochondrial respiratory flux rates. In permeabilized tumors and
209 benign mammary tissue, we assessed basal/endogenous respiration and respiration with saturating
210 carbohydrate (pyruvate/malate) and lipid (palmitoyl-carnitine) substrates. For each protocol, several
211 biological replicates (individual tumors) were utilized, spanning a continuum of whole tumor wet
212 weights/volumes **(S-Fig.5A,B)**. Since no strong correlations were found between tumor wet weight or
213 volume and basal or maximal respiration supported by carbohydrate- or lipid-linked substrates **(S-Fig.5C-**
214 **J)**, all data points were pooled. When normalizing respiration to tissue wet weight **(Fig. 7A)**, tumors
215 displayed significantly higher basal/endogenous respiration and higher respiration with subsequent
216 additions of pyruvate, malate (CI-linked respiration), ADP (State III respiration), glutamate (CI-linked
217 respiration also supported by alpha-ketoglutarate anaplerosis), and succinate (to maximize CII-linked
218 respiration) **(Fig.7B)**. Equally, tumors displayed significantly higher respiration rates supported by lipids
219 (palmitoyl-carnitine, **Fig.7C**), suggesting that HER2-driven tumors are capable of relying on both substrate
220 sources, perhaps to maximize aerobic metabolism. This initial analysis of respiratory rates was normalized
221 to tissue wet weight, which can be influenced by differences in total and mitochondrial protein content in
222 a given tissue volume. To address this, we first normalized respiratory flux rates to total cellular protein
223 **(Fig.7D,E),** which minimizes differences in factors such as tissue density and hydration that are not directly
224 contributing to mitochondrial oxygen consumption. The third normalization method employed was
225 normalizing respiratory flux to a mitochondrial enrichment factor (MEF) (**Fig.7F,G)** which is the ratio of
226 mitochondrial proteins to the underlying total proteome **(S-Fig.3B)**. This approach controls for differences
227 in mitochondrial content between tissues to determine whether increases in respiration are due to
228 increases in mitochondrial content or intrinsic changes in mitochondrial function. Interestingly, the
229 fundamental observation of increased respiratory flux rates in tumors compared to benign tissues was
230 conserved independent of the normalization method, suggesting that HER2-driven mammary tumors are
231 characterized by high respiratory flux rates independent of total cellular protein or reduced mitochondrial
232 protein content. While greater intrinsic OXPHOS was observed with all substrates, lipid supported
233 respiration was stimulated to a greater extent in the tumors, resulting in comparable carbohydrate
234 (pyruvate, malate, ADP) and lipid (palmitoyl-carnitine, malate, ADP) supported respiration **(Fig.8A)**. This
235 effect occurred despite many of the genes and proteins involved in lipid metabolism at the plasma
236 membrane and in the cytosol (e.g. *Acsl1, Adipoq, Dgat1/2, Lipe, Fabp4, Cd36, Pparg*) and mitochondria
237 (*e.g. Etfa, Etfb, Etfdh, Hadh, Hadhb, Cpt1b, Cpt2*) being downregulated in tumors compared to benign
238 mammary tissue **(Fig.8B-E)**. The intrinsic activation of respiration was not a ubiquitous finding for all
239 processes linked to OXPHOS, as reactive oxygen species (**S-Fig.6A**) emission rates were higher in tumors
240 compared to benign tissue when normalized to wet weight **(S-Fig.6B)**, lower when normalized to total
241 protein **(S-Fig.6C)** and not different when normalized to mitochondrial content **(S-Fig.6D)**.

242 **High respiratory flux rates cannot be explained by OXPHOS uncoupling**

243 Typically, respiratory capacity correlates with mitochondrial content in fully differentiated tissues[31].
244 However, given the apparent discrepancy between mitochondrial/OXPHOS protein content and
245 respiratory flux rates in HER2-driven tumors, we investigated alternative explanations for this observation.
246 One possible explanation for the observed enhanced respiratory rates could be due to the uncoupling of
247 OXPHOS from ATP synthesis, especially when ROS emission is not proportional to respiratory flux. To

248 address this possibility, we utilized oligomycin (OMY) to inhibit the F_0 subunit of ATP synthase (Complex V)
249 and examine its inhibitory potency between groups **(Fig.8F)**. While OMY inhibited respiration in benign
250 mammary tissue by ~55%, respiration in tumors was inhibited by ~80% **(Fig.8G)**. Subsequent additions of
251 antimycin A (AMA) to inhibit Complex III and rotenone (ROT) to inhibit Complex I, fully inhibited respiration
252 in both tissues **(Fig.8G)**. Since respiration was inhibited to a greater extent in the tumors in response to
253 OMY, this protocol strongly suggests that HER2-driven tumor mitochondria are highly coupled.

254 **Tumor mitochondria display altered morphology**

255 When assessing the subcellular ultrastructure of HER2-driven mammary tumors using transmission
256 electron microscopy (TEM), we observed smaller, more punctate mitochondria in tumors compared to
257 benign tissue **(Fig.9A)**. To determine whether ultrastructural observations aligned with the expression of
258 genes and proteins involved in mitochondrial turnover, we filtered our transcriptomic and proteomic
259 dataset using MitoCarta, specifically investigating mitochondrial proteins involved in mitochondrial
260 dynamics and mitophagy. This approach revealed the upregulation of several genes and proteins involved
261 in mitochondrial fission and generally a downregulation of genes and proteins involved in mitochondrial
262 fusion (**Fig.9B-F**). Together, these data show morphological differences in tumor versus benign tissue
263 mitochondria, which could potentially influence OXPHOS efficiency.

264 **HER2 inhibition supresses tumor respiration**

265 Although the exact mechanism(s) driving OXPHOS activation despite reductions in mitochondrial content
266 in our model remain unclear, we next asked whether HER2 activity directly regulates mitochondrial
267 bioenergetics. To address this, we used NF639 cells—an epithelial line derived from mammary tumors
268 from MMTV-c-neu transgenic mice, which, like our MMTV/neu^{ndl}-YD5 model, display upregulated murine
269 HER2/neu signaling[32–35] serving as a highly relevant cell-line analog to our intact tumor measurements.
270 NF639 cells were treated with lapatinib, a dual HER2/EGFR tyrosine kinase inhibitor **(Fig.10A)** a well-
271 described and validated inhibitor of HER2-mediated signaling[29,36,37]. Cells were exposed to 250nM lapatinib
272 for 24 hours, a dose and time regimen that was validated and did not notably compromise viability
273 **(Fig.10B).** Using the same CI+CII linked respirometry protocol applied to the murine tumors **(Fig.7B),**
274 lapatinib significantly reduced leak respiration, CI-linked respiration, and CI+CII-supported respiration
275 relative to DMSO-treated cells **(Fig.10C)**. Importantly, lapatinib did not induce a cytochrome c (CC)
276 response (% change in respiration with CC, CON=-0.83%, LAP=-2.9%) and did not alter respiratory
277 inhibition with OMY, AMA, or ROT **(Fig.10C)**, indicating that mitochondrial integrity and coupling were
278 maintained. Collectively, these findings demonstrate that upregulated HER2-signaling directly stimulates
279 mitochondrial bioenergetics.

280

281 **DISCUSSION**

282 The aim of the current study was to investigate the metabolic characteristics of a mouse model of HER2-
283 driven mammary cancer compared to benign mammary tissue. Specifically, we focused on the
284 bioenergetic adaptations that have occurred with HER2-driven tumorigenesis both with respect to
285 mitochondrial function (respiration and ROS) and mitochondrial content (total mitochondrial proteome
286 and OXPHOS complexes). This investigation revealed several findings: 1) HER2-driven mammary tumors
287 exhibit high respiratory rates compared to benign mammary tissue, 2) tumors are capable of oxidizing
288 lipids and pyruvate to a similar extent despite the downregulation of several genes involved in lipid
289 catabolism, 3) high tumor respiration rates cannot be explained by higher mitochondrial content, and, 4)
290 HER2 signaling regulates the upregulation of tumor respiration. These data highlight that HER2-driven
291 mammary tumors exhibit high OXPHOS rates despite lower mitochondrial content, challenging the typical
292 bioenergetic relationship in fully differentiated tissues.

293 **Relationship between mitochondrial content and function in breast cancer**

Studies simultaneously assessing mitochondrial content and mitochondrial respiration, and the contribution of these factors to breast cancer malignant transformation are scarce. While reductions in ETC subunit content/activity have been described in mitochondria isolated from human mammary carcinoma cultures compared to mammary epithelial cells[38], it has been assumed that a reduction in ETC subunit content would manifest as a reduction in respiratory capacity. However, this is at odds with several reports that classify breast cancer cells as OXPHOS reliant due to increases in mitochondrial respiration correlating with advanced disease[19,39,40]. Indeed, across many cancers it is generally assumed that mitochondrial content and respiratory function increase or decrease concomitantly, however, recent work has challenged this dogma, demonstrating that high rates of respiration normalized to tissue weight can be negated when corrected for mitochondrial mass,[41,42] revealing intrinsic alterations in cancer cell bioenergetics. In the current study, utilizing this same approach to control for differences in mitochondrial content, we found that respiratory capacity supported by pyruvate and lipids in HER2-driven mammary tumors was significantly higher (~2-4 fold) compared to benign mammary tissue despite lower mitochondrial enrichment (total mitochondrial proteome) and lower abundance of several respiratory complex subunits, suggesting mitochondrial content independent increases in mitochondrial respiratory capacity are acquired during HER2-driven tumorigenesis. This is a key finding independent of the specific mechanisms underlying the enhanced bioenergetics.

While the exact mechanisms underlying the activation of OXPHOS in the current work remain unclear, our findings allow us to speculate on several possibilities that could enhance respiration in a mitochondrial-content–independent manner. It is unlikely these factors are mutually exclusive and include increased coupling of electron transfer to ATP synthesis (coupling efficiency), changes in the delivery of substrates across the mitochondrial membranes, intrinsic changes in the activity of ETC complexes and/or ATP synthase, alterations in mitochondrial morphology/dynamics and signaling events linked to HER2 activation.

Possible mitochondrial content-independent mechanisms supporting enhanced respiration rates in HER2-driven mammary cancer

Coupling Efficiency: Several studies have suggested that a key function of mitochondrial respiration in cancer cells is the regeneration of NAD^+, FAD and ubiquinone to provide the necessary metabolites for biomass production, rather than ATP synthesis[5,6,43]. From a bioenergetic perspective, this could be achieved by inducing uncoupled respiration, which could manifest in an apparent increase in intrinsic mitochondrial respiration, given that measures of respiratory flux quantify oxygen consumption rather than ATP synthesis. However, in the present study the Complex V inhibitor oligomycin inhibited respiration to a greater extent in HER2-driven tumors, suggesting that uncoupling cannot explain the enhanced respiration rates observed, and if anything, tumors are more coupled than benign mammary tissue. This interpretation aligns with work in MCF7 cells where mitochondrial ATP represents the majority of cellular ATP production[44] suggesting the ATP synthetic function of OXPHOS in breast cancer is likely intact. Indeed, enhanced mitochondrial ATP provision and OXPHOS-dependent biomass expansion are not mutually exclusive processes and increased coupled respiration would satisfy both the bioenergetic and biosynthetic requirements of rapid cell proliferation during tumorigenesis.

Substrate Delivery and Preference: Recent work has highlighted the dependency of HER2+ tumor cells on both lipid (long chain fatty acids) and carbohydrate-derived (pyruvate) substrate for optimal proliferative capacity[45]. In addition to pyruvate, HER2-driven tumors may be particularly poised to utilize lipids, given the proximity of cancer cells to adipocytes in the mammary tumor microenvironment[46], which has spurred interest in inhibiting lipid use/fat oxidation as an adjunct therapy in HER2-driven cancer[45]. Indeed, the use of endogenous substrate may be preferred as solid tumors expand and factors such as increased interstitial fluid pressure and extracellular matrix remodelling impact tumor vessel quality[47], possibly limiting exogenous substrate delivery. However, at the transcript and protein level, enzymes involved in mitochondrial lipid uptake (CPT1, CPT2) and pyruvate uptake (MPC) were largely downregulated compared to benign tissue which would limit rather than enhance mitochondrial substrate delivery. Despite this lower abundance of enzymes supporting mitochondrial substrate delivery, mitochondrial

respiration supported by pyruvate and lipids were significantly higher in tumors. Considering lipid and carbohydrate oxidation converge within the mitochondrial matrix, both providing acetyl-CoA to the TCA cycle, it is possible that enhanced OXPHOS efficiency lies at a distal site, implicating intrinsic OXPHOS adaptations as a possible explanation for enhanced respiration in HER2-driven tumors.

Intrinsic OXPHOS Adaptations: Several cancers are characterized by the altered expression of individual ETC subunits and/or ATP synthase which can have functional repercussions on respiratory function[10,41]. In the current study, despite a consistent downregulation of subunits comprising Complexes I-IV in HER2-driven tumors, a subset of Complex V genes were not downregulated (specifically two subunits of the c-ring of F_0 domain (*Atp5g1, Atp5g2*), two subunits of the F6 domain stalk connecting the F_0 and F_1 domains (*Atp5j1, Atp5j2*), and regulatory proteins ATPase inhibitory factor 1 (*Atpif1*) and distal membrane assembly component 2 (*Dmac2l*)). This shift essentially increases the ratio of ATP synthase/ETC and raises the possibility that a maintenance of these subunits may enhance OXPHOS rates in the face of downregulated CI-IV subunit content since maximal coupled respiration is usually limited by proton flux through ATP synthase. Interestingly this observation was further supported by our assessment of scRNA-seq data in human breast tumors, where CV expression was generally uniformly and highly expressed across major cell types, further supporting the notion that the maintenance of CV may be important for tumorigenesis. Indeed, despite mtDNA lesions in proton pumping complexes (CI, CIII and CIV) being common in many cancers, presumably reducing the content/function of these complexes, ATP synthase mutations are less common, suggesting positive selection may exist to maintain coupled respiration and ATP production[10,48,49]. Thus, while speculative, it is possible that higher respiration rates in HER2-driven tumors may partially reflect maintained ATP synthase content/function.

While bioenergetic efficiency is typically related to intrinsic changes in OXPHOS stoichiometry, mitochondrial morphology can indirectly affect efficiency. We observed smaller, punctate mitochondria in HER2-driven mammary tumors when visualized by TEM, generally aligning with reductions in mitochondrial fusion and increases in mitochondrial fission-related targets. While the direct relationship between mitochondrial morphology and bioenergetics remains contentious, evidence suggests smaller mitochondria (due to enhanced fission or reduced fusion) may be associated with enhanced bioenergetics. Smaller mitochondria tend to have a higher surface-area-to-volume ratio which has been correlated with upregulated OXPHOS in the liver[50], and low rates of respiration is associated with the inhibition of mitochondrial fission[51]. Furthermore, rare genetic mitochondrial diseases are often characterized by hyper-fused mitochondria which is associated with OXPHOS limitations[52]. Indeed, morphological differences in breast cancer mitochondria are well described[16,53–55]and targeting mitochondrial dynamics for therapy is an active area of study[56–58], however, there is a clear need to ascertain the relationship between mitochondrial dynamics and bioenergetics in tumorigenesis.

Intrinsic activation of OXPHOS mediated by HER2

No matter the mechanisms underlying our observed bioenergetic activation in HER2-driven tumors, our experiments in NF639 cells demonstrate that HER2 activation appears to regulate respiratory function. Although findings in the literature regarding how HER2 activation or suppression influences mitochondrial content and bioenergetics remain mixed, several lines of evidence support the idea that HER2 is important for tumorigenesis and respiratory competence[19,59–61]. Importantly, these studies collectively reinforce that changes in mitochondrial content alone cannot fully account for alterations in respiratory function, suggesting that HER2 may regulate intrinsic mitochondrial activity. Independent groups have shown that HER2 may localize to the inner mitochondrial membrane and directly interact with respiratory complexes (CI,CIV,CV) influencing their activity[19,59,60]. Alternatively, indirect activation of bioenergetics via HER2 signaling is another possibility – which is supported by work showing mitochondrial ADP availability may be enhanced via mitochondrial creatine kinase (MtCK) phosphorylation by HER2 downstream effectors[61]. Both mechanisms would alter bioenergetics without necessarily altering mitochondrial content, which aligns with our observation that content markers do not scale with respiratory capacity. Nonetheless, further research is required to more clearly delineate the relationship between HER2 signaling, OXPHOS

activation and possible mitochondrial content independent mechanisms conferring respiratory competence.

CONCLUSION

We provide evidence that HER2-driven mammary tumors display enhanced respiratory capacity despite lower mitochondrial content. This increased respiratory capacity could not be explained by changes in OXPHOS coupling, however, differences in mitochondrial morphology and the maintained expression of several subunits of ATP synthase suggest HER2-driven mammary tumors may undergo intrinsic adaptations in mitochondrial function during tumorigenesis. No matter the mechanism driving OXPHOS activation in our model, upregulated HER2 signaling is essential for the observed increases in mitochondrial respiratory capacity.

MATERIALS AND METHODS

Animals and Breeding

All rodent experiments were conducted in accordance with institutional guidelines approved by the Animal Care Committee at the University of Guelph (AUP#5071). MMTV/*neu*^{ndl}-YD5 mice on an FVB background were obtained from Dr. William Muller (McGill University) and Dr. David Ma (University of Guelph). Female MMTV/*neu*^{ndl}-YD5 mice were obtained by breeding male heterozygous MMTV/*neu*^{ndl}-YD5 mice with female FVB mice to yield WT or heterozygous transgenics. Mice were group housed in ventilated cages at room temperature (22ºC) and kept on a 12:12 light-dark cycle with *ad libitum* access to a chow diet and water. Starting at 10 weeks, mice were monitored for tumor development on a biweekly basis for ~10 additional weeks. Mice with tumors exceeding 17 mm in length/width or a volume over 5000 m^3 were euthanized before the 20-week time point.

Tumor and Benign Mammary Tissue Collection

Mice were anesthetized using sodium pentobarbital (60 mg/kg body weight) and checked for depth of anaesthesia by leg retraction after tail pinch. Once under the surgical plane, a ventral incision was made up the midline and the skin separated bilaterally from the underlying fascia to allow for the excision of the intact mammary tumors. Depending on the number of tumors present (typically 1-5), tumors were allocated for mitochondrial function (placed fresh in BIOPS preservation buffer), histology (TEM: fixed in 2.5% glutaraldehyde/1% paraformaldehyde, IF: fixed in 10% formalin) or snap frozen in liquid nitrogen for further analysis (western blotting, transcriptomics, quantitative label-free proteomics) immediately after whole tumor wet weight was recorded. Paired mammary tissue with no visible tumors, furthest from the site of tumor excision (i.e. if tumors localized in cervical region benign tissue was harvested from inguinal region) were used as an internal comparison, denoted as benign mammary tissue. While mitochondrial respiration experiments were performed in paired tissue (benign and tumor from same mouse), transcriptomic, proteomic and histological analyses were performed on tumors and benign samples from different mice due to tissue limitations.

RNA Sequencing and Transcriptomic Analyses

Frozen tissues were homogenized and lysed in TRIzol reagent. After centrifuging, the supernatant (aqueous phase) was applied to the RNeasy kit (Qiagen, 74106) for subsequent total RNA extraction and purification in accordance with the manufacturer's protocol. RNA samples were sent to the McMaster Genomics Facility where an RNA quality check, poly A enrichment, library prep and quality check were performed as previously described[62]. These samples were then run in an Illumina Nextseq P2, 2x50bp sequencing run. FastQC and MultiQC were used for quality control of raw data. Salmon's transcript-level quantification[63] and DESeq2[64] was used to detect DEGs with the threshold of adjusted p-value<0.1. PCA

438 analysis was performed by using variance stabilizing transformation (VST) data through DESeq2 using the
439 pcaExplorer package[65] in R (version 4.2.1). Functional enrichment analysis was performed by GO
440 enrichment analysis[66] and Kyoto Encyclopedia of Genes and Genomes (KEGG) mapping using the GOstats,
441 KEGG.db, and Bioconductor packages. Heatmaps and volcano plots were generated with ggplot2 package
442 using all detected genes or genes sorted by an adjusted p-value<0.1 by false discovery rate method.
443 Detailed descriptions for each analysis are included in the figure descriptions.

444 **Western Blotting**

445 Tumor and benign mammary tissues were homogenized in lysis buffer, diluted to equal protein
446 concentration (1 µg/uL), separated by SDS-PAGE, transferred onto PVDF membranes and detected using
447 enhanced chemiluminescence (ChemiGenius2 Bioimaging System, SynGene, Cambridge, UK) as previously
448 described[67,68]. Commercially available primary antibodies were used to detect total and phosphorylated
449 targets (p38 MAPK (CS9212S, 1:1000), ERK1/2 (CS9102S, 1:1000), Akt (CS4691S, 1:1000), mTOR (CS2972S,
450 1:1000), p70s6k1 (CS9202S, 1:1000), eEf2 (CS2332S, 1:1000), p-p38 MAPK (CS9211S, 1:1000), p-ERK1/2
451 (CS9101S, 1:1000), p-AKT (CS9271S, 1:1000), p-mTOR (CS2971S, 1:1000), p-p70s6k1 (CS9234S, 1:1000), p-
452 eEF2 (CS2331S, 1:1000), OXPHOS complexes CII and CIV (Ab110413, 1:1000)). Due to rapid tissue/protein
453 turnover in tumor tissues, Ponceau staining was an inappropriate loading control, however, trends in total
454 protein targets between groups aligned with quantitative label-free proteomic analyses as a secondary
455 method measuring protein content, validating targets detected by western blotting.

456 **Protein Extraction and Purification for LC-MS**

457 A Bradford assay was used to determine the protein concentration in the samples. Twenty-five µg of
458 protein per lysate was resolubilized with denaturation buffer (6M urea/2M thiourea) and concurrently
459 reduced with 10 mM DTT and alkylated with 20 mM iodoacetamide at RT for 60 min. Samples were
460 precipitated by adding 6:1 v/v cold acetone and kept at -80°C for 60 minutes and the pellet was collected
461 after centrifugation at 10,000g for 10 min at 4°C. Samples were resuspended with 50 mM ammonium
462 bicarbonate and MD-grade trypsin (Thermo Fisher Scientific, Cat#90057) was added at a ratio of 1:50
463 protease to protein. Digestion occurred overnight at 37°C. After digestion, samples were dried by vacuum
464 centrifugation and purified using Pierce C18 Spin columns (Thermo Fisher Scientific, cat#89873).

465 **LC-MS**

466 The Vanquish Neo UHPLC system was coupled with Orbitrap Exploris 240 mass-spectrometer using the
467 Easy-Spray source for nanoLC-MS protein identification. The Vanquish Neo UHPLC system was configured
468 for trap and elute analysis. Peptides were first trapped and washed on a Pepmap Neo C18 trap column (5
469 micron, 300 micron x5 mm) then separated on EASY-Spray columns 75 µm I.D. × 50 cm with the maximum
470 pressure of 1200 bar. The nanoLC-MS system was controlled with Standard Instrument Integration (SII)
471 for Xcalibur software. All hardware and data acquisition software were from Thermo Fisher Scientific. The
472 mobile phase A and weak wash liquid was water with 0.1% FA, and the mobile phase B and strong wash
473 liquid was 80% acetonitrile with 0.1% FA. The gradient was as follows 4-19% B over 72 min, 19-29% B over
474 28 min, 29-45% B over 20 min and a 14.5 min wash at 100% B with a flow rate of 300 nL/min. The
475 autosampler temperature was 7 °C, and the column temperature was 45 °C. The sample was injected with
476 Fast Loading set to 'Enabled' with Pressure Control at 500 bar. The column Fast Equilibration function was
477 set to 'Enabled' with Pressure control at 800 bar, and the equilibration factor was set to 3. Vial bottom
478 detection was set to 'Enabled'.

479 **DDA MS Method**

480 The Orbitrap Exploris 240 MS was operated in DDA mode using a full scan with *m/z* range 375–1500,
481 Orbitrap resolution of 60 000, normalized AGC target value 300%, and maximum injection time set to
482 Auto. The intensity threshold for precursor was set to 1×10^4. MS/MS spectra starting from 120 *m/z* were

483 acquired in data-dependent acquisition (DDA) mode with a cycle time of 2 s, where the precursors were
484 isolated in a window of 1.6 Da and subsequently fragmented with HCD using a normalized collision energy
485 of 30%. Orbitrap resolution was set to 15 000 for MS2. The normalized AGC target was standard, and the
486 maximum injection time was set to Auto.

487 **Proteomics data analysis**

488 Analysis of the tissue proteome was performed in R (version 4.2.1) and R Studio (version 2024.04.2+764).
489 Principal component analysis was performed using the Vegan package. Volcano plots were created using
490 log2 transformed fold change comparing cancer/benign tissue and -log10 adjusted p-value. P-values of
491 differentially regulated proteins between each group were corrected with p.adjust (method = "fdr")
492 within each comparison. Depending on the analysis, heatmaps and volcano plots were generated using
493 all detected proteins or proteins sorted by p.adjust <0.1, detailed descriptions for each analysis are
494 included in the figure descriptions. Gene set enrichment was performed with the Kyoto Encyclopedia of
495 genes and genomes (KEGG)[69] and EnrichR[70].

496 **Cell Culture**

497 NF639 murine epithelial mammary tumor cells (ATCC: CRL-3090) were cultured in DMEM supplemented
498 with 10% fetal bovine serum (FBS; Gibco), 4 mM L-glutamine, 1 mM sodium pyruvate, 50 U/mL penicillin
499 and 50 ug/mL streptomycin (Wisent), maintained by passaging in 100 mm plates, and incubated at 37°C
500 and 5% CO_2. Cells were seeded in 96-well plates (10^4 cells/well; n=3 technical replicates) for microplate
501 viability assays or in 100 mm plates for mitochondrial respiration experiments. At 60% confluency, cells
502 were serum-starved for 6 hours, followed by lapatinib treatment (Cayman, 11493) in complete culture
503 medium containing 2% FBS for 24 hours. Cell viability in the presence of lapatinib was tested using a crystal
504 violet assay. Cells were treated with lapatinib at 0 nM, 100 nM, 250 nM, 500 nM, 1000 nM, or 5000 nM
505 for 24 hours. Following treatment incubation, cells were washed and stained with crystal violet dye
506 (Abcam) and absorbance was measured at 570 nm as per the manufacturer's instructions. Assays were
507 repeated in triplicate. For mitochondrial respiration experiments, cells were treated with 250 nM lapatinib
508 or DMSO (control) in complete culture medium containing 2% FBS for 24 hours. Cells were washed,
509 trypsinized (1x trypsin-EDTA, Wisent), and centrifuged at 300g for 5 min before counting. Cells were
510 washed and resuspended in 1x PBS and centrifuged at 300g for 5 minutes. Cells were resuspended in
511 Mir05 respiration buffer (0.5 mM EGTA, 3 mM $MgCl_2 \cdot H_2O$, 60 mM potassium lactobionate, 10 mM KH_2PO_4,
512 20 mM HEPES, 110 mM sucrose, 20 mM taurine, and 1 g/L fatty acid free BSA; pH 7.1) for mitochondrial
513 respiration.

514 **Mitochondrial Respiration**

515 Mitochondrial respiration experiments were performed using the Oroboros Oxygraph-2k systems at 37ºC
516 in MiR05 respiration with constant stirring at room air saturation (starting at 180 µM O_2). For respiration
517 experiments in intact tumors and benign tissue, 2-5 mg of permeabilized tumor tissue or 15-20 mg of
518 permeabilized (both permeabilized with 20 µg/µL saponin) mammary tissue were used per 2 mL chamber
519 and each protocol was conducted as at least two technical replicates (duplicate) per tumor or benign
520 sample. Prior to the addition of substrates for any protocol, endogenous (basal) respiration was assessed
521 with no substrates added. Complex I and Complex II supported respiration was assessed with the addition
522 of 5 mM pyruvate and 2 mM malate, 5 mM ADP, 10 mM glutamate and 10 mM succinate. This respiratory
523 capacity measurement represents supraphysiological substrate concentrations delivered in the absence of
524 diffusion limitations. In a subset of these experiments, subsequent additions of oligomycin (OMY, 1 µM),
525 antimycin A (AMA, 2.5 µM) and rotenone (ROT, 1 µM) were added to assess OXPHOS coupling. In a
526 separate protocol, lipid-supported respiration was assessed with 20 µM palmitoyl-carnitine in the
527 presence of 2 mM malate and 5 mM ADP. For respiration experiments in NF639 cells, the same respiration
528 buffers and chamber conditions were utilized. One million cells were added per technical replicate and
529 Complex I and II supported respiration was assessed using the same protocol described in intact tumors

530 and benign tissue in the presence of 20 µg digitonin to ensure permeabilization. Respiration was expressed
531 per viable cell.

532 **Reactive Oxygen Species Emission**

533 Mitochondrial hydrogen peroxide (H_2O_2) emission was determined fluorometrically (Lumina, Thermo
534 Scientific, Waltham, MA) in permeabilized mammary tissue and mammary tumors as previously
535 described[67] with minor modifications. In brief, 2-5 mg of minced tissue was loaded into a cuvette
536 containing Amplex Red (Invitrogen, Waltham, MA, USA), horseradish peroxidase (5U/mL), saponin (20
537 µg/µL), superoxide dismutase (40 U/mL) in Buffer Z (105 mM K-MES, 30 mM KCl, 1 mM EGTA, 10 mM
538 K_2HPO_4, 5 mM $MgCl_2$, 5 µM glutamate, 5 µM malate, 0.5% BSA, pH 7.4). Emission rates were assessed at
539 37ºC in the presence of 10 mM succinate and calculated using a standard curve generated with known
540 concentrations of H_2O_2.

541 **Data Normalization**

542 Mitochondrial respiration rates and H_2O_2 emission were normalized to individual sample wet weight,
543 group total protein content and group mitochondrial content (mitochondrial enrichment factor, MEF).
544 Total protein content was calculated as a group average (n=6/group) based on a Bradford assay and back-
545 calculated total protein in a given wet weight of starting tissue. Data was normalized to mitochondrial
546 protein by calculating the MEF for each group (n=g/group) based on all detected mitochondrial proteins
547 by quantitative label-free proteomics (Mouse MitoCarta 3.0 database) normalized to total protein
548 abundance per sample as previously described by others[31,42].

549

550 **Histology**

551 **Transmission Electron Microscopy:** Immediately following tissue dissection, tumor and benign mammary
552 tissues were fixed in 2.5% glutaraldehyde/1% paraformaldehyde overnight at 4ºC. The following day,
553 tissues were washed 3x in 100 mM HEPES buffer in preparation for embedding. Tissue was stained with
554 1% osmium tetroxide for 3h, washed 3x in HEPES buffer and further stained with 1% uranyl acetate for 3h
555 before washing 2x in HEPES buffer and once in ddH2O. Stained tissue was dehydrated with a graded
556 ethanol series followed by infiltration with LR White resin. Blocks were polymerized at 60ºC for 18 hours
557 before ultramicrotomy. Sections were post-stained with uranyl acetate and lead citrate. Sections were
558 allowed to fully dry before imaging on the FEI Tecnai G2 F20 transmission electron microscope operated
559 under normal conditions at 120 kVe.

560 **Immunofluorescence:** Tumor and benign samples (n=4/group) were fixed in 10% formalin for 24 hours
561 and stored in 70% ethanol at 4ºC. Samples were blocked in paraffin and sectioned, deparaffinized in
562 xylene, and rehydrated through a graded ethanol series. Samples were washed in PBS and incubated for
563 20 min in 0.02% sodium borohydride in PBS to quench endogenous phosphatase activity. Antigen retrieval
564 was performed in citrate buffer (90ºC) for 12 min, followed by a 20-min cooling period. Sections were then
565 blocked in 5% BSA in PBS for 1h to prevent nonspecific antibody binding. Primary antibodies (anti-vimentin
566 (1:100, Novus Bio NBP1-31327), anti-cytokeratin (1:100, Novus Bio NBP2-29429), anti-CD4 (1:200, Abcam
567 AB183685), anti-CD138 (1:100, StemCell Technologies 60035), anti-CD31 (1:150, Abcam AB28364), or anti-
568 CD68 (1:100, Novus Bio NB100-683)) were diluted in 1% BSA and applied overnight at 4 °C in a humidified
569 chamber. The following day, sections were incubated for 2 hours at room temperature with the
570 appropriate fluorophore-conjugated secondary antibodies (Invitrogen): Alexa Fluor 594 anti-rabbit (1:100
571 or 1:200), Alexa Fluor 488 anti-mouse (1:100), Alexa Fluor 488 anti-rat (1:200), or Alexa Fluor 488 anti-
572 rabbit (1:100). Slides were washed and mounted with ProLong™ Gold Antifade Mountant containing DAPI
573 (Thermo Fisher) and protected from light for 24 hours before being transferred to -20°C for storage. Images
574 were acquired at 40× magnification using an Olympus BX-61 epifluorescence microscope equipped with
575 Metamorph imaging software. Monochromatic images captured at 594 nm excitation were pseudocolored
576 red, while those captured at 488 nm were pseudocolored green. Staining intensity was quantified in

ImageJ using manual region-of-interest selection, and immunopositive area was expressed as a percentage of total tissue area (expressed as % immunopositive area).

OXPHOS Index and OXPHOS Score Calculations

A publicly available single-cell RNA-seq dataset from of 26 human breast tumors[31] was combined with cell-type proportion analyses from our tumor and benign tissues (see Immunofluorescence methods) to estimate cell-type-specific contribution to OXPHOS.

Using human MitoCarta 3.0, we filtered for all detected OXPHOS subunit genes in the scRNA-seq dataset. For each major cell type described in the dataset (B-, T-, plasmablasts, CAFs, PVL, endothelial, myeloid, normal epithelial, and cancer epithelial cells), we extracted the percent of cells expressing each subunit gene. These percent expression values were averaged per complex to generate a mean CI-V expression value for each cell type. To account for differences in cell-type abundance within the scRNA-seq dataset, this percent expression was multiplied by the cell-type proportion reported in the same study. In subsequent calculations, this is reported as $\%Expression_{CT}$.

To estimate cell-type-specific OXPHOS expression in our benign and tumor samples, we calculated an *OXPHOS mRNA Index* for all cell types present in both datasets (myeloid, T-, plasmablasts, endothelial, mesenchymal, and epithelial cells):

$$OXPHOS\ mRNA\ Index = (\%Expression_{CT}) * (\%Immunopositive_{CT})$$

Where, $\%Expression_{CT}$ is the average gene expression data per respiratory complex in each complementary major cell type (CT), and $\%Immunopositive_{CT}$ is cell type proportion measured by IF in our samples. This index represents how much each cell type is expected to contribute to CI-V expression in our tissues, integrating both expression and abundance.

Next, to estimate the contribution of each cell type to the OXPHOS transcriptome in the current study, the OXPHOS mRNA index in each cell type were summed to calculate a Total OXPHOS mRNA Score.

$$Total\ OXPHOS\ mRNA\ Score = \sum_{i=\mathrm{I,II,III,IV,V}} OXPHOS\ RNA\ Index\ Ci$$

Statistical Analysis

Statistical analysis and data visualization was performed using Microsoft Excel, GraphPad Prism (version 10.2.3), R (version 4.2.1) and R Studio (version 2024.04.2+764). All data are presented as mean ± SD and data was considered statistically significant if $p<0.05$. For transcriptomic and proteomic analyses, an adjusted p-value of <0.1 was utilized. Details regarding specific statistical analyses are included in the Results section and within each figure legend.

DATA AVAILABILITY

Raw RNA sequencing and proteomics data were deposited in GEO (accession number: GSE315552) and PRIDE databases (accession number: PXD071897) respectively.

ACKNOWLEDGEMENTS

This work is funded by a National Sciences and Engineering Research Council (NSERC) grant by GPH (400362). SMF is funded by an NSERC-CGS doctoral scholarship.

FIGURE LEGENDS

Figure 1. Experimental design and canonical HER2 signaling. A) Schematic of mammary tumors from the mammary fat pad of female MMTV-neu^{ndl}-YD5 mice and normal (benign) mammary tissue, representative images of tumor morphology (tumor capsule, peripheral tumor tissue and necrotic core), tissue processing workflow for transcriptomics, proteomics, western blotting, mitochondrial respiration, ROS emission, and histology (transmission electron microscopy (TEM) and immunofluorescence (IF)). **B)** Schematic of classical signaling pathways (Ras/MAPK and PI3K/AKT/mTOR) downstream of HER2 receptor stimulation in the

YD5 model. **C)** *Her2* gene expression (transcripts per million, TPM), **D)** Gene expression for canonical HER2 signaling. **E)** Absolute abundance of HER2 protein detected by quantitative label-free proteomics (n.d. = HER2 not detected in benign). **F)** Representative western blots of proteins involved in canonical HER2 signaling. **G,H)** Quantified western blots (% of benign) for **G)** total protein content and **H)** phosphorylated targets normalized to the total protein content of each target. P-values in panels **D** and **E** listed as adjusted p values from transcriptomic (DEG) data (p-adj. <0.1 considered statistically significant). In panels **G,H** data is presented as means ± SD and statistical significance was determined using an unpaired, two tailed Student's t-test (*=p<0.05, n=5-6 per group/protein target). ***Abbrev.*** *AKT - protein kinase B; eEf2 - eukaryotic elongation factor 2; eIF4E – eukaryotic translation initiation factor 4E; ERK – extracellular signal-regulated kinase; GRB2 – growth factor receptor-bound protein-2, MEK – mitogen-activated protein kinase kinase; mTORC1/2 – mechanistic target of rapamycin complex 1 and 2; PDK – 3-phosphoinositide-dependent protein kinase-1; PI3K – phosphoinositide 3-kinase; PIP2/3 – phosphatidylinositol 4,5 bisphosphate, PIP3 – phosphatidylinositol 3,4,5-triphosphate; p70S6k1 – ribosomal protein S6 kinase beta-1; RAF – rapidly accelerated fibrosarcoma; RAS – rate sarcoma virus; SHC – Src homolog and collagen homolog; 4EBP1 – eukaryotic translation initiation factor 4E-binding protein 1.*

Figure 2. Assessment of HER2-driven mammary tumor and benign mammary tissue transcriptomes. A) PCA of benign mammary tissue and mammary tumors, **B)** Volcano plot showing differentially expressed genes (DEGs) identified between mammary tissue and mammary tumors. **C)** Heatmap of top 3000 DEGs, **D)** Top 10 upregulated pathways (Reactome 2022) and **E)** gene ontologies (GO Biological Process 2023) in tumors compared to benign mammary tissue, **F)** Top 10 downregulated pathways (Reactome 2022) and **G)** gene ontologies (GO Biological Process 2023) in tumors compared to benign mammary tissue. Panels **D,E** assess the top 3000 upregulated DEGs (log2fc>1), panels **F,G** assess the top 3000 downregulated DEGs (log2fc<1). An adjusted p-value of <0.1 was considered statistically significant across all analyses. The Enrichr open access analysis web tool was used to generate panels **D-G** which were sorted by p-value.

Figure 3. Assessment of HER2-driven mammary tumor and benign mammary tissue proteomes. A) Venn diagram showing all detected proteins. Of the 1848 overlapping targets, 420 were significantly different based on a p-adj. <0.1 and 411 of those proteins were downregulated in tumors. **B)** PCA of benign mammary samples and mammary tumors, **C)** Volcano plot showing proteins identified between mammary tumors and benign mammary tissue, those in blue (downregulated) or red (upregulated) were significantly different (n=420 proteins, p-adj. <0.1). **D)** Heatmap of 420 differentially expressed proteins in benign and tumor samples. **E)** Top 10 downregulated pathways (Reactome 2022) and **F)** gene ontologies (GO Biological Process, 2023), **G)** KEGG analysis of downregulated proteins. The Enrichr open access analysis web tool was used to generate panels **E,F** which were sorted by p-value.

Figure 4. Overlapping genes and proteins between HER2-driven mammary tumor transcriptome and proteome. Correlation of log2FC for overlapping targets between the HER2-driven tumor and benign mammary tissue transcriptomes and proteomes grouped by up/downregulation **A),** and **B)** protein localization (mitochondrial vs other). **C)** Venn diagram showing 144 overlapping downregulated targets between the assessed HER2-driven tumor and benign mammary tissue transcriptomes and proteomes. **D)** KEGG analysis for common downregulated targets. Top 10 downregulated **E)** pathways (Reactome 2022) and **F)** gene ontologies (GO Biological Process 2023). An adjusted p value of <0.1 was utilized for all analyses. The Enrichr open access analysis web tool was used to generate panels **E,F** which were sorted by p-value.

Figure 5. Assessment of the mitochondrial transcriptome and proteome. A) Venn diagram showing mitochondrial proteins detected in the current dataset when cross-referenced with the Mouse MitoCarta 3.0 database. **B)** Heatmap of 125 mitochondrial proteins identified in benign mammary tissue and HER2-driven tumors (n=5/group). **C)** Absolute abundance of all mitochondrial proteins detected in benign and tumor tissues. **D)** Gene expression (detected by transcriptomics; transcripts per million) of all detected OXPHOS subunits separated per respiratory complex, black and white bars represent subunits with no significant differences between groups. **E-J)** Heatmaps of **E)** Complex I, **F)** Complex II, **G)** Complex III, **H)** Complex IV, **I)** Complex V (ATP synthase) and **J)** TCA cycle transcriptomes. All proteomic analyses **(panels A-C)** were conducted on n=5/group. All transcriptomic analyses **(panels D-J)** were conducted on n=6/group. **Panels B,C** were analyzed using an unpaired two tailed Student's t-test (*p<0.05). In **Panel D**, * and coloured (blue and green bars) represent significant differences between benign and tumor samples based on an adjusted p value of <0.1. OXPHOS complex schematics in panel **D** were obtained from the open access RCSB Protein Data Bank *(Complex I = TW1V, Complex II=2A06, Complex III= 3SFD Complex IV=6NMP Complex V = 5FIL). Bars in panel **D** are listed in the following order: Complex I: Ndufa1, Ndufa10, Ndufa11, Ndufa12, Ndufa13, Ndufa2, Ndufa3, Ndufa5, Ndufa6, Ndufa7, Ndufa8, Ndufa9, Ndufab1, Ndufb10, Ndufb11, Ndufb2, Ndufb3, Ndufb4, Ndufb5, Ndufb6, Ndufb7, Ndufb8, Ndufb9, Ndufc1, Ndufc2, Ndufs1, Ndufs2, Ndufs3, Ndufs4, Ndufs5, Ndufs6, Ndufs7, Ndufs8, Ndufv1, Ndufv2, Ndufv3; Complex II: Sdha, Sdhb, Sdhc, Sdhd; Complex III: Cyc1, Uqcr10, Uqcr11, Uqcrb, Uqcrc1, Uqcrc2, Uqcrfs1, Uqcrh, Uqcrq; Complex IV: Cox4i1, Cox4i2, Cox5a, Cox5b, Cox6a1, Cox6b1, Cox6b2, Cox6c, Cox7a1, Cox7a2, Cox7a2l, Cox7b, Cox7c, Cox8a, Cox8b, Ndufa4; Complex V: Atp5a1, Atp5b, Atp5c1, Atp5d, Atp5e, Atp5g1, Atp5g2, Atp5g3, Atp5h, Atp5j, Atp5j2, Atp5k, Atp5l, Atp5md, Atp5mpl, Atp5o, Atp5pb, Atpif1, Dmac2l.*

Figure 6. Cell type specific OXPHOS mRNA analysis in benign and tumor samples. A) OXPHOS expression per cell type from a publicly available single-cell RNA sequencing dataset[31] shown as a dot plot for each respiratory complex (Complexes I-V) subunit that was detected. Dot size indicates the percentage of cells of a given major type expressing each subunit gene (% cells expressing). Dot color represents gene expression scaled relative to each gene's expression distribution across all major cell types. **B)** Percentage of cells expressing OXPHOS subunits, arranged in ascending order per cell type for Complexes I-V. **C)** Representative immunofluorescence images of benign mammary tissue and tumor samples stained for vimentin, cytokeratin, CD68, CD31, CD4 and CD138. **D)** Quantification of cell-type proportion (% immunopositive area) in benign and tumor samples. **E)** OXPHOS mRNA

Index calculated for Complexes I-V. $OXPHOS\ mRNA\ Index = (\%Expression_{CT}) * (\%Immunopositive_{CT})$ where CT represents cell type. **F)** Total OXPHOS mRNA Score for each cell type. $TOTAL\ OXPHOS\ mRNA\ Score = \sum_{i=\mathrm{I,II,III,IV,V}} OXPHOS\ mRNA\ Index\ Ci$. Where *i* represents mitochondrial respiratory complexes.

Figure 7. Assessment of lipid and carbohydrate linked mitochondrial respiration and OXPHOS coupling in benign mammary tissue and HER2-driven mammary tumors. A) Schematic depicting methods of normalization for respiration rates (*per wet weight, total protein, mitochondrial protein/enrichment*). **B)** Complex I and complex II- supported respiration normalized to tissue wet weight, **C)** lipid-supported respiration normalized to tissue wet weight, **D)** Complex I and complex II-supported respiration normalized to total protein content, **E)** lipid-supported respiration normalized to total protein content, **F)** Complex I and complex II-supported respiration normalized to mitochondrial protein (mitochondrial enrichment factor, MEF). **G)** Lipid supported respiration normalized to mitochondrial protein. All individual values represent biological replicates (n=9-22/group depending on the protocol). Data are presented as means ± SD, statistical analyses were conducted using an unpaired, two-tailed Student's t-test (*p<0.05). ***Abbrev:*** *E = Endogenous, PM = pyruvate (5 mM), malate (2 mM), D = ADP (5 mM), G = glutamate (10 mM), S = succinate (10 mM), PC = palmitoyl-carnitine (20 µM), CI+CII = maximal CI+CII-supported respiration (PMDGS).*

Figure 8. Lipid and carbohydrate linked respiration and lipid metabolism transcriptome and proteome. A) Rates of carbohydrate (pyruvate, malate, ADP) and lipid (palmitoyl-carnitine, malate, ADP) supported respiration in tumors and benign mammary tissue. **B)** Gene expression (transcripts per million) of mitochondrial pyruvate carrier and carnitine palmitoyltransferase isoforms mediating mitochondrial pyruvate and long chain fatty acid transport respectively. **C)** Network interaction showing downregulated (unsupervised analysis) gene clustering in the HER2-driven tumor transcriptome, **D)** Heatmap of differentially expressed genes involved in lipid oxidation. **E)** Heatmap of differentially expressed proteins involved in lipid metabolism. **F)** Representative trace of protocol used to assess mitochondrial coupling. Following maximal rates of complex I and II- supported respiration, 1 µM oligomycin (OMY) was added to inhibit Complex V (ATP synthase), followed by 2.5 µM antimycin-A (AMA) and 1 µM rotenone (ROT) to inhibit complexes III and I respectively. **G)** Group data for experiment depicted in **(F)** depicted as relative inhibition from maximal complex I and II supported respiration (PMDGS) in each group. In panels **A, B, F** and **G** data are presented as means ± SD and statistical analyses were conducted using an unpaired, two-tailed Student's t-test (*p<0.05).

Figure 9. Mitochondrial morphology and assessment of mitochondrial fusion, mitochondrial fission and mitophagy transcriptomes and proteomes in benign mammary tissue and HER2-driven tumors. A) Transmission electron microscopy (TEM) images of tumor and benign samples showing punctate (tumor) versus elongated (benign) mitochondria. **B)** Gene expression (detected by transcriptomics; transcripts per million) of fusion, fission and mitophagy related genes separated per process filtered by MitoCarta, coloured bars and * represent genes with an adjusted p value of <0.1. Black and white bars represent genes with no significant differences between groups. **C)** Heatmap of fusion transcriptome, **D)** Heatmap of fusion proteome, **E)** Heatmap of fission transcriptome, **F)** Heatmap of fission proteome, **G)** Heatmap of mitophagy transcriptome, **H)** Heatmap of mitophagy proteome. TEM images are from independent tumor and benign tissue samples. Heatmaps depict all detected proteins (n=5/group) and transcripts (n=6/group).

Figure 10. Mitochondrial respiration is supressed by tyrosine kinase inhibitor lapatinib. A) Schematic showing mechanism of lapatinib mediated inhibition of HER2 tyrosine kinase activity. **B)** NF639 cell viability assessed using a crystal violet assay expressed as a percentage of untreated viability (0nM lapatinib). **C)** Complex I and II supported respiration in the presence of 20µg digitonin in NF639 cells untreated (grey) or treated with 250 nM lapatinib for 24h. Left inset: Schematic of substrates supporting Complex I-II respiration, schematic of lapatinib or DMSO treatment. Right inset: Percent inhibition of maximal CI+II supported respiration (PMDGSC) with OMY, AMA and ROT. Following maximal rates of complex I and II- supported respiration, 1 µM oligomycin (OMY) was added to inhibit Complex V (ATP synthase), followed by 2.5 µM antimycin-A (AMA) and 1 µM rotenone (ROT) to inhibit complexes III and I respectively. Each datapoint represents a technical replicate (duplicate) and data are presented as means ± SD. Statistical analyses were conducted using an unpaired, two-tailed Student's t-test (*p<0.05). ***Abbrev:*** *E = Endogenous, PMD = pyruvate (5 mM), malate (2 mM), D= ADP (5 mM), G = glutamate (10 mM), S = succinate (10 mM), CC = cytochrome C (10 µM).*

Supplementary Figure 1. Absolute phosphorylated protein targets downstream of HER2 activation. A) Quantified western blots for phosphorylated canonical HER2 signaling proteins (n=5-6/group). Phosphorylation sites are indicated for each target. **B)** Representative blot for each phosphorylated target. Data are presented as mean ± SD and analyzed with an unpaired, two tailed Student's t-test (*p<0.05).

Supplementary Figure 2. Unique HER2-driven tumor and benign mammary tissue proteins. A) Venn diagram depicting 741 and 600 unique proteins identified in benign mammary tissue and HER2-driven tumors respectively, **B)** KEGG analysis of all detected unique benign mammary tissue proteins, **C)** Top 10 pathways (Reactome 2022), **D)** Top 10 gene ontologies (GO Biological Process) in benign mammary tissue, **E)** KEGG analysis of unique HER2-driven tumor proteins, **F)** Top 10 pathways (Reactome 2022), **G)** Top 10 gene ontologies (GO Biological Process) in HER2-driven tumors. KEGG, pathway and GO analyses were conducted on all mammary and tumor proteins detected by quantitative label-free proteomics. The Enrichr open access analysis web tool was used to generate panels **C,D,F and G** which were sorted by p-value.

Supplementary Figure 3. Mitochondrial enrichment in benign mammary tissue and HER2-driven mammary tumors. A) Total and mitochondrial (Mouse MitoCarta 3.0) absolute protein abundance assessed by quantitative label-free proteomics. **B)** Mitochondrial enrichment factor (MEF) calculated as the ratio of all detected MitoCarta proteins relative to the underlying total

proteome per sample (n=5/group). Statistical analysis was conducted using an unpaired two tailed Student's t-test (*p<0.05). In panel **A**, *# denotes significant differences between both total and MitoCarta proteomes between groups.

Supplementary Figure 4. Proteomic analysis of detected OXPHOS subunits. Heatmaps showing subunits detected for **A)** Complex I, **B)** Complex II, **C)** Complex III, **D)** Complex IV, **E)** Complex V (ATP synthase) using quantified label-free proteomics. **F)** OXPHOS Complex I-V absolute abundance as a percentage of the mitochondrial proteome (n=5/group). **G)** OXPHOS complex I-V absolute abundance as a percentage of the total detected proteome (n=5/group). **H)** Representative and quantified western blots for Complex II and Complex IV expressed as percentage of benign. Data in panels **F,G,H** are presented as means ± SD and analyzed with an unpaired, two tailed Student's t-test (*p<0.05).

Supplementary Figure 5. Correlation of tumor size and volume with maximal carbohydrate and lipid-supported respiration rates. A) Tumor wet weight (whole tumor post excision), **B)** Tumor volume calculated as a modified ellipse ($V=1/2(length*width^2)$). **C-F)** Endogenous (no substrate, CI+CII protocol), Endogenous (no substrate, lipid protocol), State 3 (5 mM pyruvate, 2 mM malate, 5 mM ADP) and maximal lipid-supported (2 mM malate, 5 mM ADP, 20 µM palmitoyl-carnitine) respiration rates correlated with tissue wet weight. **G-J**) Same respiration data as **(C-F)** but correlated with tumor volume. The Pearson correlation coefficient (R) values are listed for each correlation.

Supplementary Figure 6. Reactive oxygen species emission in benign mammary tissue and HER2-driven mammary tumors. A) Schematic depicting major sites of superoxide (O_2^{*-}) emission from respiratory complexes I and III. Superoxide dismutase 2 (SOD2) subsequently catalyzes the dismutation of O_2^{*-} into hydrogen peroxide (H_2O_2) which can be measured fluorometrically. **B)** H_2O_2 emission per wet tissue weight, **C)** H_2O_2 emission per total protein, **D)** H_2O_2 emission per mitochondrial protein (MEF, mitochondrial enrichment factor). Statistical analyses were conducted using an unpaired, two-tailed Student's t-test (*p<0.05).

Supplementary Table 1. List of 9 significantly upregulated proteins between tumor and benign samples, sorted in order of fold change from benign (smallest to largest fold change). General pathways or functions are listed per protein based on ID mapping from the Uniprot protein sequence database. Adjusted p-values are listed per target.

REFERENCES

1. Vasan, K., Werner, M., and Chandel, N.S. (2020). Mitochondrial Metabolism as a Target for Cancer Therapy. Cell Metab. *32*, 341–352. https://doi.org/10.1016/j.cmet.2020.06.019.

2. DeBerardinis, R.J., and Chandel, N.S. (2020). We need to talk about the Warburg effect. Nat. Metab. *2*, 127–129. https://doi.org/10.1038/s42255-020-0172-2.

3. Warburg, O. (1924). Über den Stoffwechsel der Carcinomzelle. Naturwissenschaften *12*, 1131–1137. https://doi.org/10.1007/BF01504608.

4. Warburg, O. (1956). On respiratory impairment in cancer cells. Science *124*, 269–270.

5. Sullivan, L.B., Gui, D.Y., Hosios, A.M., Bush, L.N., Freinkman, E., and Vander Heiden, M.G. (2015). Supporting Aspartate Biosynthesis Is an Essential Function of Respiration in Proliferating Cells. Cell *162*, 552–563. https://doi.org/10.1016/j.cell.2015.07.017.

6. Martínez-Reyes, I., Cardona, L.R., Kong, H., Vasan, K., McElroy, G.S., Werner, M., Kihshen, H., Reczek, C.R., Weinberg, S.E., Gao, P., et al. (2020). Mitochondrial ubiquinol oxidation is necessary for tumour growth. Nature *585*, 288–292. https://doi.org/10.1038/s41586-020-2475-6.

7. Morris, J.P., Yashinskie, J.J., Koche, R., Chandwani, R., Tian, S., Chen, C.-C., Baslan, T., Marinkovic, Z.S., Sánchez-Rivera, F.J., Leach, S.D., et al. (2019). α-Ketoglutarate links p53 to cell fate during tumour suppression. Nature *573*, 595–599. https://doi.org/10.1038/s41586-019-1577-5.

8. Sciacovelli, M., Guzzo, G., Morello, V., Frezza, C., Zheng, L., Nannini, N., Calabrese, F., Laudiero, G., Esposito, F., Landriscina, M., et al. (2013). The mitochondrial chaperone TRAP1

781 promotes neoplastic growth by inhibiting succinate dehydrogenase. Cell Metab. *17*, 988–
782 999. https://doi.org/10.1016/j.cmet.2013.04.019.

783 9. Cardaci, S., Zheng, L., MacKay, G., van den Broek, N.J.F., MacKenzie, E.D., Nixon, C.,
784 Stevenson, D., Tumanov, S., Bulusu, V., Kamphorst, J.J., et al. (2015). Pyruvate carboxylation
785 enables growth of SDH-deficient cells by supporting aspartate biosynthesis. Nat. Cell Biol.
786 *17*, 1317–1326. https://doi.org/10.1038/ncb3233.

787 10. Smith, A.L., Whitehall, J.C., Bradshaw, C., Gay, D., Robertson, F., Blain, A.P., Hudson, G., Pyle,
788 A., Houghton, D., Hunt, M., et al. (2020). Age-associated mitochondrial DNA mutations
789 cause metabolic remodelling that contributes to accelerated intestinal tumorigenesis. Nat.
790 Cancer *1*, 976–989. https://doi.org/10.1038/s43018-020-00112-5.

791 11. Tan, A.S., Baty, J.W., Dong, L.-F., Bezawork-Geleta, A., Endaya, B., Goodwin, J., Bajzikova, M.,
792 Kovarova, J., Peterka, M., Yan, B., et al. (2015). Mitochondrial genome acquisition restores
793 respiratory function and tumorigenic potential of cancer cells without mitochondrial DNA.
794 Cell Metab. *21*, 81–94. https://doi.org/10.1016/j.cmet.2014.12.003.

795 12. Weinberg, F., Hamanaka, R., Wheaton, W.W., Weinberg, S., Joseph, J., Lopez, M.,
796 Kalyanaraman, B., Mutlu, G.M., Budinger, G.R.S., and Chandel, N.S. (2010). Mitochondrial
797 metabolism and ROS generation are essential for Kras-mediated tumorigenicity. Proc. Natl.
798 Acad. Sci. U. S. A. *107*, 8788–8793. https://doi.org/10.1073/pnas.1003428107.

799 13. Yuan, Y., Ju, Y.S., Kim, Y., Li, J., Wang, Y., Yoon, C.J., Yang, Y., Martincorena, I., Creighton, C.J.,
800 Weinstein, J.N., et al. (2020). Comprehensive molecular characterization of mitochondrial
801 genomes in human cancers. Nat. Genet. *52*, 342–352. https://doi.org/10.1038/s41588-019-
802 0557-x.

803 14. Wang, Z., Zheng, Z., Jia, S., Liu, S., Xiao, X., Chen, G., Liang, W., and Lu, X. (2022).
804 Trastuzumab resistance in HER2-positive breast cancer: Mechanisms, emerging biomarkers
805 and targeting agents. Front. Oncol. *12*.

806 15. Avagliano, A., Ruocco, M.R., Aliotta, F., Belviso, I., Accurso, A., Masone, S., Montagnani, S.,
807 and Arcucci, A. (2019). Mitochondrial Flexibility of Breast Cancers: A Growth Advantage and
808 a Therapeutic Opportunity. Cells *8*, 401. https://doi.org/10.3390/cells8050401.

809 16. Baek, M.L., Lee, J., Pendleton, K.E., Berner, M.J., Goff, E.B., Tan, L., Martinez, S.A., Mahmud,
810 I., Wang, T., Meyer, M.D., et al. (2023). Mitochondrial structure and function adaptation in
811 residual triple negative breast cancer cells surviving chemotherapy treatment. Oncogene *42*,
812 1117–1131. https://doi.org/10.1038/s41388-023-02596-8.

813 17. Evans, K.W., Yuca, E., Scott, S.S., Zhao, M., Paez Arango, N., Cruz Pico, C.X., Saridogan, T.,
814 Shariati, M., Class, C.A., Bristow, C.A., et al. (2021). Oxidative Phosphorylation Is a Metabolic
815 Vulnerability in Chemotherapy-Resistant Triple-Negative Breast Cancer. Cancer Res. *81*,
816 5572–5581. https://doi.org/10.1158/0008-5472.CAN-20-3242.

817 18. El-Botty, R., Morriset, L., Montaudon, E., Tariq, Z., Schnitzler, A., Bacci, M., Lorito, N., Sourd,
818 L., Huguet, L., Dahmani, A., et al. (2023). Oxidative phosphorylation is a metabolic
819 vulnerability of endocrine therapy and palbociclib resistant metastatic breast cancers. Nat.
820 Commun. *14*, 4221. https://doi.org/10.1038/s41467-023-40022-5.

19. Rohlenova, K., Sachaphibulkij, K., Stursa, J., Bezawork-Geleta, A., Blecha, J., Endaya, B., Werner, L., Cerny, J., Zobalova, R., Goodwin, J., et al. (2017). Selective Disruption of Respiratory Supercomplexes as a New Strategy to Suppress Her2high Breast Cancer. Antioxid. Redox Signal. *26*, 84–103. https://doi.org/10.1089/ars.2016.6677.

20. Yap, T.A., Daver, N., Mahendra, M., Zhang, J., Kamiya-Matsuoka, C., Meric-Bernstam, F., Kantarjian, H.M., Ravandi, F., Collins, M.E., Francesco, M.E.D., et al. (2023). Complex I inhibitor of oxidative phosphorylation in advanced solid tumors and acute myeloid leukemia: phase I trials. Nat. Med. *29*, 115–126. https://doi.org/10.1038/s41591-022-02103-8.

21. Mun, S., Lee, H.J., and Kim, P. (2024). Rebuilding the microenvironment of primary tumors in humans: a focus on stroma. Exp. Mol. Med. *56*, 527–548. https://doi.org/10.1038/s12276-024-01191-5.

22. de Visser, K.E., and Joyce, J.A. (2023). The evolving tumor microenvironment: From cancer initiation to metastatic outgrowth. Cancer Cell *41*, 374–403. https://doi.org/10.1016/j.ccell.2023.02.016.

23. Ursini-Siegel, J., Schade, B., Cardiff, R.D., and Muller, W.J. (2007). Insights from transgenic mouse models of ERBB2-induced breast cancer. Nat. Rev. Cancer *7*, 389–397. https://doi.org/10.1038/nrc2127.

24. Iqbal, N., and Iqbal, N. (2014). Human Epidermal Growth Factor Receptor 2 (HER2) in Cancers: Overexpression and Therapeutic Implications. Mol. Biol. Int. *2014*, 1–9. https://doi.org/10.1155/2014/852748.

25. Dankort, D.L., Wang, Z., Blackmore, V., Moran, M.F., and Muller, W.J. (1997). Distinct Tyrosine Autophosphorylation Sites Negatively and Positively Modulate Neu-Mediated Transformation. Mol. Cell. Biol. *17*, 5410–5425. https://doi.org/10.1128/MCB.17.9.5410.

26. Dankort, D., Jeyabalan, N., Jones, N., Dumont, D.J., and Muller, W.J. (2001). Multiple ErbB-2/Neu Phosphorylation Sites Mediate Transformation through Distinct Effector Proteins. J. Biol. Chem. *276*, 38921–38928. https://doi.org/10.1074/jbc.M106239200.

27. Ruiz-Saenz, A., Dreyer, C., Campbell, M.R., Steri, V., Gulizia, N., and Moasser, M.M. (2018). HER2 amplification in tumors activates PI3K/Akt signaling independent of HER3. Cancer Res. *78*, 3645–3658. https://doi.org/10.1158/0008-5472.CAN-18-0430.

28. Kirouac, D.C., Du, J., Lahdenranta, J., Onsum, M.D., Nielsen, U.B., Schoeberl, B., and McDonagh, C.F. (2016). HER2+ Cancer Cell Dependence on PI3K vs. MAPK Signaling Axes Is Determined by Expression of EGFR, ERBB3 and CDKN1B. PLoS Comput. Biol. *12*, e1004827. https://doi.org/10.1371/journal.pcbi.1004827.

29. Serra, V., Scaltriti, M., Prudkin, L., Eichhorn, P.J.A., Ibrahim, Y.H., Chandarlapaty, S., Markman, B., Rodriguez, O., Guzman, M., Rodriguez, S., et al. (2011). PI3K inhibition results in enhanced HER signaling and acquired ERK dependency in HER2-overexpressing breast cancer. Oncogene *30*, 2547–2557. https://doi.org/10.1038/onc.2010.626.

30. Boykov, I.N., Montgomery, M.M., Hagen, J.T., Aruleba, R.T., McLaughlin, K.L., Coalson, H.S., Nelson, M.A., Pereyra, A.S., Ellis, J.M., Zeczycki, T.N., et al. (2023). Pan-tissue mitochondrial phenotyping reveals lower OXPHOS expression and function across cancer types. Sci. Rep. *13*, 16742. https://doi.org/10.1038/s41598-023-43963-5.

31. Wu, S.Z., Al-Eryani, G., Roden, D.L., Junankar, S., Harvey, K., Andersson, A., Thennavan, A., Wang, C., Torpy, J.R., Bartonicek, N., et al. (2021). A single-cell and spatially resolved atlas of human breast cancers. Nat. Genet. *53*, 1334–1347. https://doi.org/10.1038/s41588-021-00911-1.

32. Amundadottir, L.T., and Leder, P. (1998). Signal transduction pathways activated and required for mammary carcinogenesis in response to specific oncogenes. Oncogene *16*, 737–746. https://doi.org/10.1038/sj.onc.1201829.

33. Muller, W.J., Sinn, E., Pattengale, P.K., Wallace, R., and Leder, P. (1988). Single-step induction of mammary adenocarcinoma in transgenic mice bearing the activated c-neu oncogene. Cell *54*, 105–115. https://doi.org/10.1016/0092-8674(88)90184-5.

34. Min, C., Kirsch, K.H., Zhao, Y., Jeay, S., Palamakumbura, A.H., Trackman, P.C., and Sonenshein, G.E. (2007). The Tumor Suppressor Activity of the Lysyl Oxidase Propeptide Reverses the Invasive Phenotype of Her-2/neu–Driven Breast Cancer. Cancer Res. *67*, 1105–1112. https://doi.org/10.1158/0008-5472.CAN-06-3867.

35. Romieu-Mourez, R., Landesman-Bollag, E., Seldin, D.C., and Sonenshein, G.E. (2002). Protein kinase CK2 promotes aberrant activation of nuclear factor-kappaB, transformed phenotype, and survival of breast cancer cells. Cancer Res. *62*, 6770–6778.

36. Xiang, Z., Song, S., Zhu, Z., Sun, W., Gifts, J.E., Sun, S., Li, Q.S., Yu, Y., and Li, K.K. (2019). LncRNAs GIHCG and SPINT1-AS1 Are Crucial Factors for Pan-Cancer Cells Sensitivity to Lapatinib. Front. Genet. *10*, 25. https://doi.org/10.3389/fgene.2019.00025.

37. Leung, W., Roxanis, I., Sheldon, H., Buffa, F.M., Li, J., Harris, A.L., and Kong, A. (2015). Combining lapatinib and pertuzumab to overcome lapatinib resistance due to NRG1-mediated signalling in HER2-amplified breast cancer. Oncotarget *6*, 5678–5694. https://doi.org/10.18632/oncotarget.3296.

38. Putignani, L., Raffa, S., Pescosolido, R., Aimati, L., Signore, F., Torrisi, M.R., and Grammatico, P. (2008). Alteration of expression levels of the oxidative phosphorylation system (OXPHOS) in breast cancer cell mitochondria. Breast Cancer Res. Treat. *110*, 439–452. https://doi.org/10.1007/s10549-007-9738-x.

39. Hu, Y., Xu, W., Zeng, H., He, Z., Lu, X., Zuo, D., Qin, G., and Chen, W. (2020). OXPHOS-dependent metabolic reprogramming prompts metastatic potential of breast cancer cells under osteogenic differentiation. Br. J. Cancer *123*, 1644–1655. https://doi.org/10.1038/s41416-020-01040-y.

40. Pacheco-Velázquez, S.C., Robledo-Cadena, D.X., Hernández-Reséndiz, I., Gallardo-Pérez, J.C., Moreno-Sánchez, R., and Rodríguez-Enríquez, S. (2018). Energy Metabolism Drugs Block Triple Negative Breast Metastatic Cancer Cell Phenotype. Mol. Pharm. *15*, 2151–2164. https://doi.org/10.1021/acs.molpharmaceut.8b00015.

41. Nelson, M.A., McLaughlin, K.L., Hagen, J.T., Coalson, H.S., Schmidt, C., Kassai, M., Kew, K.A., McClung, J.M., Neufer, P.D., Brophy, P., et al. (2021). Intrinsic OXPHOS limitations underlie cellular bioenergetics in leukemia. eLife *10*, e63104. https://doi.org/10.7554/eLife.63104.

42. McLaughlin, K.L., Hagen, J.T., Coalson, H.S., Nelson, M.A.M., Kew, K.A., Wooten, A.R., and Fisher-Wellman, K.H. (2020). Novel approach to quantify mitochondrial content and intrinsic bioenergetic efficiency across organs. Sci. Rep. *10*, 17599. https://doi.org/10.1038/s41598-020-74718-1.

43. Luengo, A., Li, Z., Gui, D.Y., Sullivan, L.B., Zagorulya, M., Do, B.T., Ferreira, R., Naamati, A., Ali, A., Lewis, C.A., et al. (2021). Increased demand for NAD+ relative to ATP drives aerobic glycolysis. Mol. Cell *81*, 691-707.e6. https://doi.org/10.1016/j.molcel.2020.12.012.

44. Giddings, E.L., Champagne, D.P., Wu, M.-H., Laffin, J.M., Thornton, T.M., Valenca-Pereira, F., Culp-Hill, R., Fortner, K.A., Romero, N., East, J., et al. (2021). Mitochondrial ATP fuels ABC transporter-mediated drug efflux in cancer chemoresistance. Nat. Commun. *12*, 2804. https://doi.org/10.1038/s41467-021-23071-6.

45. Nandi, I., Ji, L., Smith, H.W., Avizonis, D., Papavasiliou, V., Lavoie, C., Pacis, A., Attalla, S., Sanguin-Gendreau, V., and Muller, W.J. (2024). Targeting fatty acid oxidation enhances response to HER2-targeted therapy. Nat. Commun. *15*, 6587. https://doi.org/10.1038/s41467-024-50998-3.

46. Wang, Y.Y., Attané, C., Milhas, D., Dirat, B., Dauvillier, S., Guerard, A., Gilhodes, J., Lazar, I., Alet, N., Laurent, V., et al. Mammary adipocytes stimulate breast cancer invasion through metabolic remodeling of tumor cells. JCI Insight *2*, e87489. https://doi.org/10.1172/jci.insight.87489.

47. Matuszewska, K., Pereira, M., Petrik, D., Lawler, J., and Petrik, J. (2021). Normalizing Tumor Vasculature to Reduce Hypoxia, Enhance Perfusion, and Optimize Therapy Uptake. Cancers *13*, 4444. https://doi.org/10.3390/cancers13174444.

48. Wu, S., Akhtari, M., and Alachkar, H. (2018). Characterization of Mutations in the Mitochondrial Encoded Electron Transport Chain Complexes in Acute Myeloid Leukemia. Sci. Rep. *8*, 13301. https://doi.org/10.1038/s41598-018-31489-0.

49. Schöpf, B., Weissensteiner, H., Schäfer, G., Fazzini, F., Charoentong, P., Naschberger, A., Rupp, B., Fendt, L., Bukur, V., Giese, I., et al. (2020). OXPHOS remodeling in high-grade prostate cancer involves mtDNA mutations and increased succinate oxidation. Nat. Commun. 2020 111 *11*, 1–16. https://doi.org/10.1038/s41467-020-15237-5.

50. Zhou, Y., Long, D., Zhao, Y., Li, S., Liang, Y., Wan, L., Zhang, J., Xue, F., and Feng, L. (2022). Oxidative stress-mediated mitochondrial fission promotes hepatic stellate cell activation via stimulating oxidative phosphorylation. Cell Death Dis. *13*, 1–15. https://doi.org/10.1038/s41419-022-05088-x.

51. Lhuissier, C., Desquiret-Dumas, V., Girona, A., Alban, J., Faure, J., Cassereau, J., Codron, P., Lenaers, G., Baris, O.R., Gueguen, N., et al. (2024). Mitochondrial F0F1-ATP synthase governs the induction of mitochondrial fission. iScience *27*. https://doi.org/10.1016/j.isci.2024.109808.

52. Zou, W., Chen, Q., Slone, J., Yang, L., Lou, X., Diao, J., and Huang, T. (2021). Nanoscopic quantification of sub-mitochondrial morphology, mitophagy and mitochondrial dynamics in living cells derived from patients with mitochondrial diseases. J. Nanobiotechnology *19*, 136. https://doi.org/10.1186/s12951-021-00882-9.

53. Ren, K., Zhou, D., Wang, M., Li, E., Hou, C., Su, Y., Zou, Q., Zhou, P., and Liu, X. (2021). RACGAP1 modulates ECT2-Dependent mitochondrial quality control to drive breast cancer metastasis. Exp. Cell Res. *400*, 112493. https://doi.org/10.1016/j.yexcr.2021.112493.

54. Zhao, J., Zhang, J., Yu, M., Xie, Y., Huang, Y., Wolff, D.W., Abel, P.W., and Tu, Y. (2013). Mitochondrial dynamics regulates migration and invasion of breast cancer cells. Oncogene *32*, 4814–4824. https://doi.org/10.1038/onc.2012.494.

55. Han, X.-J., Yang, Z.-J., Jiang, L.-P., Wei, Y.-F., Liao, M.-F., Qian, Y., Li, Y., Huang, X., Wang, J.-B., Xin, H.-B., et al. (2015). Mitochondrial dynamics regulates hypoxia-induced migration and antineoplastic activity of cisplatin in breast cancer cells. Int. J. Oncol. *46*, 691–700. https://doi.org/10.3892/ijo.2014.2781.

56. Zamberlan, M., Boeckx, A., Muller, F., Vinelli, F., Ek, O., Vianello, C., Coart, E., Shibata, K., Christian, A., Grespi, F., et al. (2022). Inhibition of the mitochondrial protein Opa1 curtails breast cancer growth. J. Exp. Clin. Cancer Res. CR *41*, 95. https://doi.org/10.1186/s13046-022-02304-6.

57. Yin, M., Lu, Q., Liu, X., Wang, T., Liu, Y., and Chen, L. (2016). Silencing Drp1 inhibits glioma cells proliferation and invasion by RHOA/ ROCK1 pathway. Biochem. Biophys. Res. Commun. *478*, 663–668. https://doi.org/10.1016/j.bbrc.2016.08.003.

58. Tang, Q., Liu, W., Zhang, Q., Huang, J., Hu, C., Liu, Y., Wang, Q., Zhou, M., Lai, W., Sheng, F., et al. (2018). Dynamin-related protein 1-mediated mitochondrial fission contributes to IR-783-induced apoptosis in human breast cancer cells. J. Cell. Mol. Med. *22*, 4474–4485. https://doi.org/10.1111/jcmm.13749.

59. Novotna, E., Milosevic, M., Prukova, D., Magalhaes-Novais, S., Dvorakova, S., Dmytruk, K., Gemperle, J., Zudova, D., Nickl, T., Vrbacky, M., et al. (2024). Mitochondrial HER2 stimulates respiration and promotes tumorigenicity. Eur. J. Clin. Invest. *54*, e14174. https://doi.org/10.1111/eci.14174.

60. Ding, Y., Liu, Z., Desai, S., Zhao, Y., Liu, H., Pannell, L.K., Yi, H., Wright, E.R., Owen, L.B., Dean-Colomb, W., et al. (2012). Receptor tyrosine kinase ErbB2 translocates into mitochondria and regulates cellular metabolism. Nat. Commun. *3*, 1271. https://doi.org/10.1038/ncomms2236.

61. Kurmi, K., Hitosugi, S., Yu, J., Boakye-Agyeman, F., Wiese, E.K., Larson, T.R., Dai, Q., Machida, Y.J., Lou, Z., Wang, L., et al. (2018). Tyrosine Phosphorylation of Mitochondrial Creatine Kinase 1 Enhances a Druggable Tumor Energy Shuttle Pathway. Cell Metab. *28*, 833-847.e8. https://doi.org/10.1016/j.cmet.2018.08.008.

62. Wang, D., Townsend, L.K., DesOrmeaux, G.J., Frangos, S.M., Batchuluun, B., Dumont, L., Kuhre, R.E., Ahmadi, E., Hu, S., Rebalka, I.A., et al. (2023). GDF15 promotes weight loss by

enhancing energy expenditure in muscle. Nature *619*, 143–150. https://doi.org/10.1038/s41586-023-06249-4.

63. Patro, R., Duggal, G., Love, M.I., Irizarry, R.A., and Kingsford, C. (2017). Salmon provides fast and bias-aware quantification of transcript expression. Nat. Methods *14*, 417–419. https://doi.org/10.1038/nmeth.4197.

64. Love, M.I., Huber, W., and Anders, S. (2014). Moderated estimation of fold change and dispersion for RNA-seq data with DESeq2. Genome Biol. *15*, 550. https://doi.org/10.1186/s13059-014-0550-8.

65. Marini, F., and Binder, H. (2019). pcaExplorer: an R/Bioconductor package for interacting with RNA-seq principal components. BMC Bioinformatics *20*, 331. https://doi.org/10.1186/s12859-019-2879-1.

66. Mi, H., Muruganujan, A., Huang, X., Ebert, D., Mills, C., Guo, X., and Thomas, P.D. (2019). Protocol Update for large-scale genome and gene function analysis with the PANTHER classification system (v.14.0). Nat. Protoc. *14*, 703–721. https://doi.org/10.1038/s41596-019-0128-8.

67. Paglialunga, S., Ludzki, A., Root-McCaig, J., and Holloway, G.P. (2015). In adipose tissue, increased mitochondrial emission of reactive oxygen species is important for short-term high-fat diet-induced insulin resistance in mice. Diabetologia *58*, 1071–1080. https://doi.org/10.1007/s00125-015-3531-x.

68. Miotto, P.M., and Holloway, G.P. (2019). Exercise-induced reductions in mitochondrial ADP sensitivity contribute to the induction of gene expression and mitochondrial biogenesis through enhanced mitochondrial H2O2 emission. Mitochondrion *46*, 116–122. https://doi.org/10.1016/j.mito.2018.03.003.

69. Kanehisa, M., Sato, Y., Kawashima, M., Furumichi, M., and Tanabe, M. (2016). KEGG as a reference resource for gene and protein annotation. Nucleic Acids Res. *44*, D457–D462. https://doi.org/10.1093/nar/gkv1070.

70. Xie, Z., Bailey, A., Kuleshov, M.V., Clarke, D.J.B., Evangelista, J.E., Jenkins, S.L., Lachmann, A., Wojciechowicz, M.L., Kropiwnicki, E., Jagodnik, K.M., et al. (2021). Gene Set Knowledge Discovery with Enrichr. Curr. Protoc. *1*, e90. https://doi.org/10.1002/cpz1.90.

Figure 1

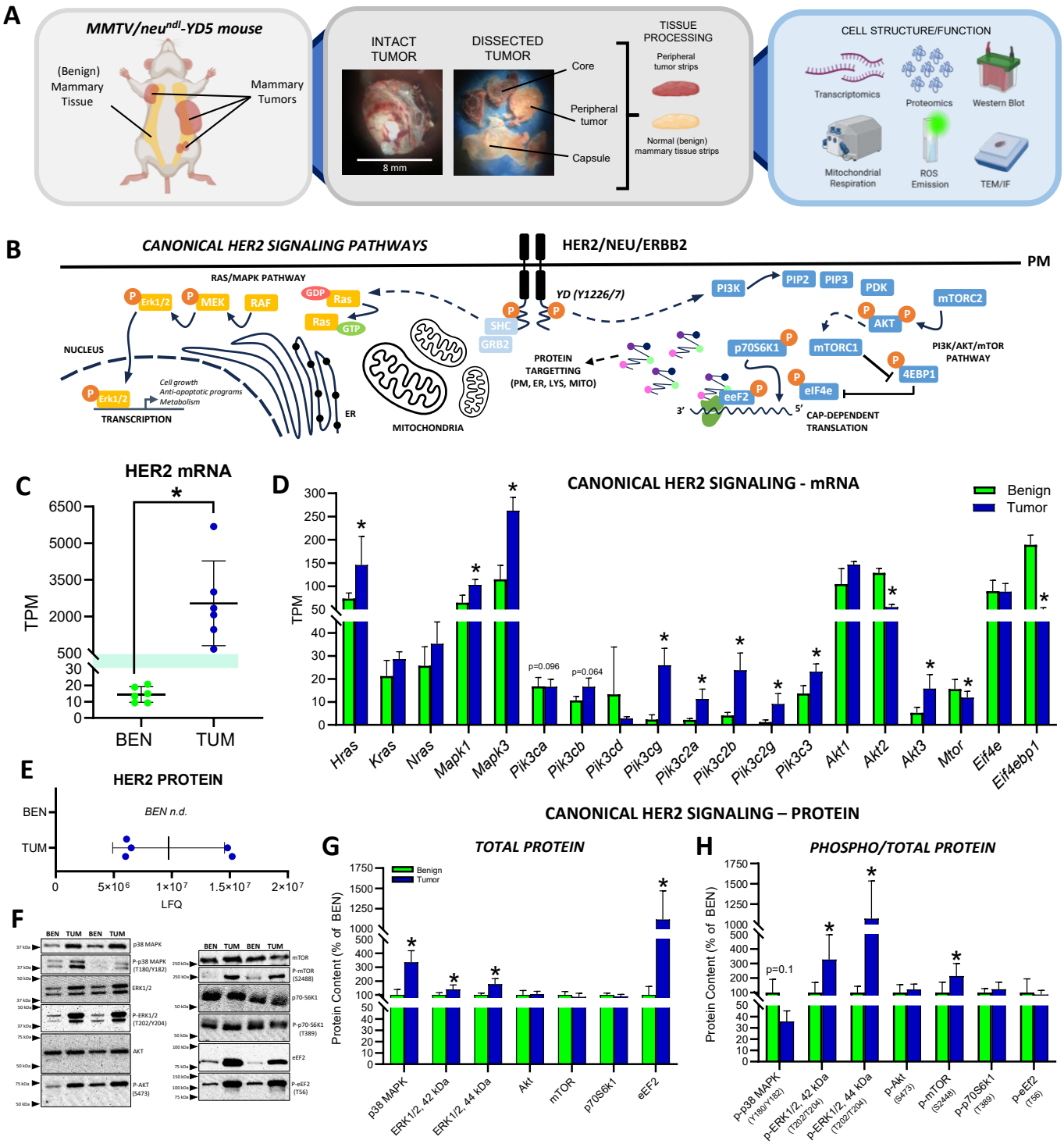
A
MMTV/neu^ndl-YD5 mouse
(Benign) Mammary Tissue
Mammary Tumors
INTACT TUMOR
DISSECTED TUMOR
8 mm
Core
Peripheral tumor
Capsule
TISSUE PROCESSING
Peripheral tumor strips
Normal (benign) mammary tissue strips
CELL STRUCTURE/FUNCTION
Transcriptomics
Proteomics
Western Blot
Mitochondrial Respiration
ROS Emission
TEM/IF
B
CANONICAL HER2 SIGNALING PATHWAYS
HER2/NEU/ERBB2
PM
RAS/MAPK PATHWAY
Erk1/2
MEK
RAF
GDP
Ras
GTP
NUCLEUS
Cell growth
Anti-apoptotic programs
Metabolism
TRANSCRIPTION
ER
MITOCHONDRIA
SHC
GRB2
YD (Y1226/7)
PROTEIN TARGETTING (PM, ER, LYS, MITO)
PI3K
PIP2
PIP3
PDK
mTORC2
AKT
p70S6K1
mTORC1
4EBP1
PI3K/AKT/mTOR PATHWAY
eeF2
eIF4e
3'
5'
CAP-DEPENDENT TRANSLATION
C
HER2 mRNA
TPM
BEN
TUM
D
CANONICAL HER2 SIGNALING - mRNA
Benign
Tumor
p=0.096
p=0.064
Hras
Kras
Nras
Mapk1
Mapk3
Pik3ca
Pik3cb
Pik3cd
Pik3cg
Pik3c2a
Pik3c2b
Pik3c2g
Pik3c3
Akt1
Akt2
Akt3
Mtor
Eif4e
Eif4ebp1
E
HER2 PROTEIN
BEN n.d.
LFQ
F
BEN TUM BEN TUM
p38 MAPK
P-p38 MAPK (T180/Y182)
ERK1/2
P-ERK1/2 (T202/Y204)
AKT
P-AKT (S473)
mTOR
P-mTOR (S2488)
p70-S6K1
P-p70-S6K1 (T389)
eEF2
P-eEF2 (T56)
CANONICAL HER2 SIGNALING – PROTEIN
G
TOTAL PROTEIN
Protein Content (% of BEN)
p38 MAPK
ERK1/2, 42 kDa
ERK1/2, 44 kDa
Akt
mTOR
p70S6k1
eEF2
H
PHOSPHO/TOTAL PROTEIN
p=0.1
p-p38 MAPK (Y180/Y182)
p-ERK1/2, 42 kDa (T202/T204)
p-ERK1/2, 44 kDa (T202/T204)
p-Akt (S473)
p-mTOR (S2448)
p-p70S6K1 (T389)
p-eEF2 (T56)

Figure 2

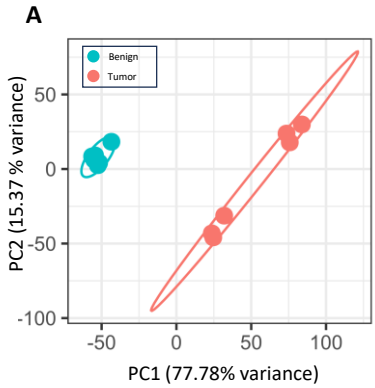

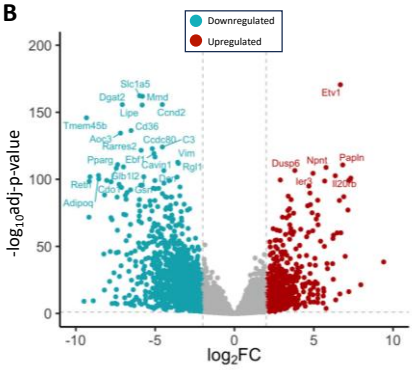

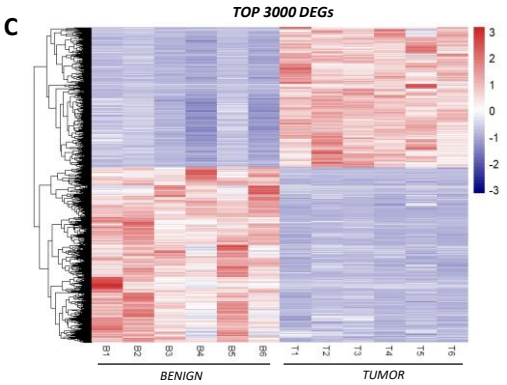

TOP 3000 UPREGULATED DEGs

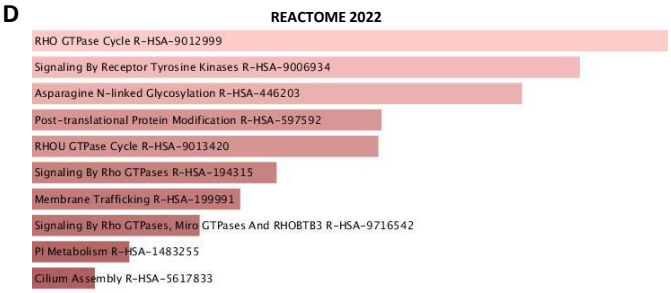

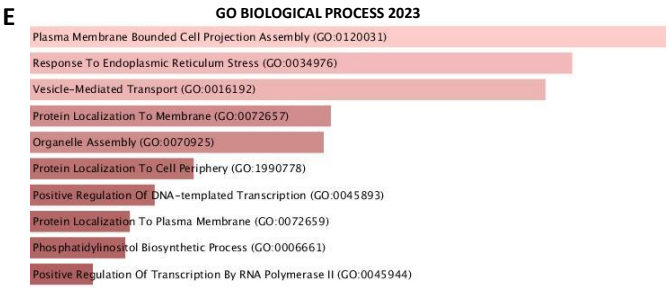

TOP 3000 DOWNREGULATED DEGs

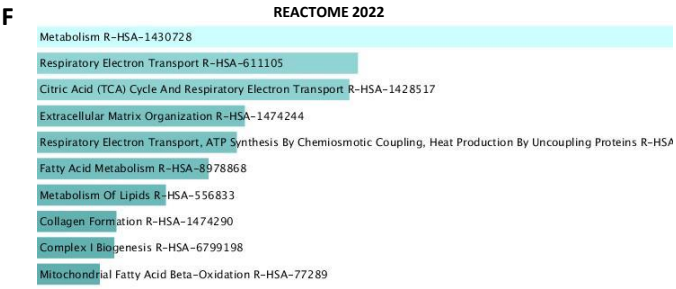

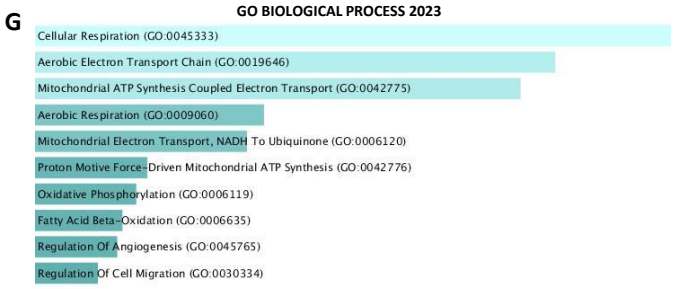

Figure 3

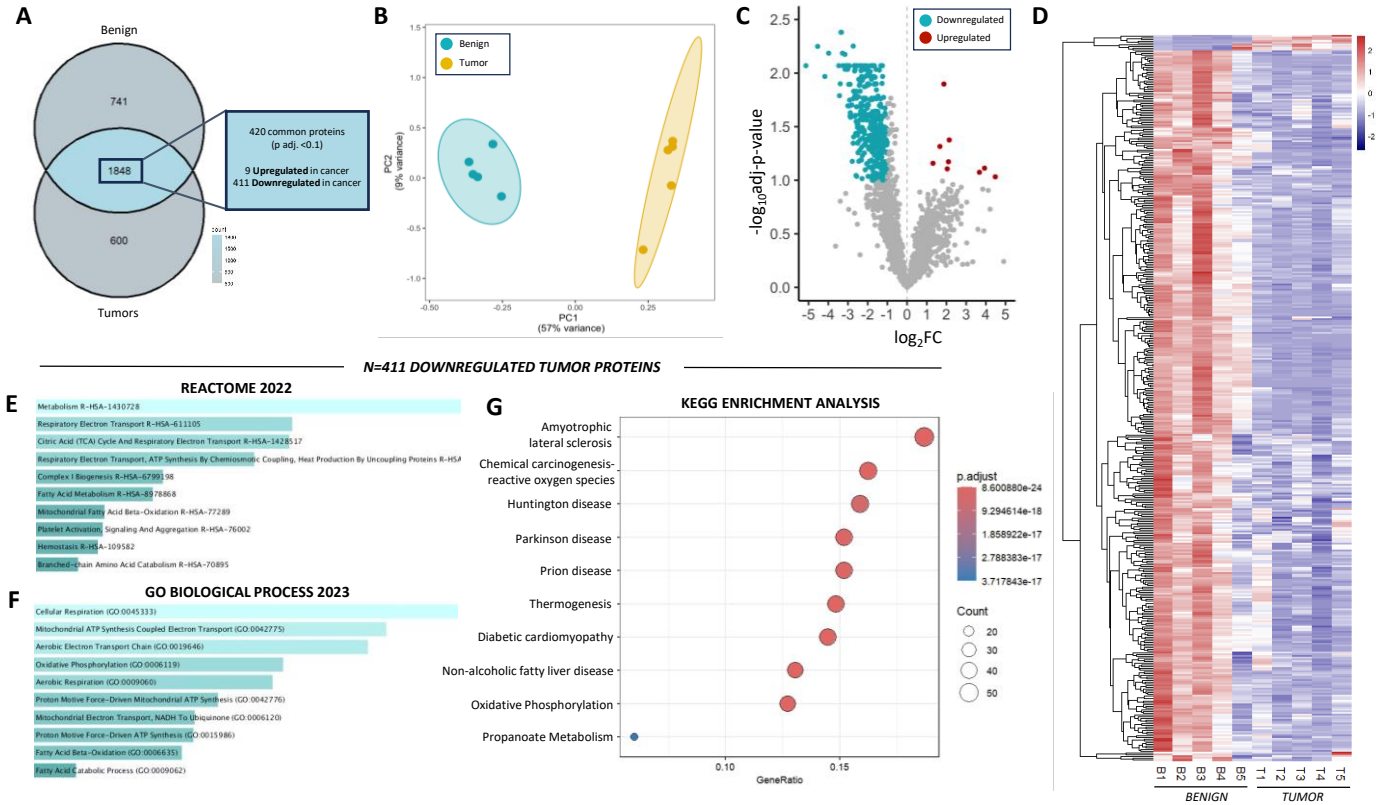
A
Benign
741
1848
600
Tumors
420 common proteins
(p adj. <0.1)
9 Upregulated in cancer
411 Downregulated in cancer
B
Benign
Tumor
PC2
(9% variance)
PC1
(57% variance)
C
Downregulated
Upregulated
-log10adj-p-value
log2FC
D
B1
B2
B3
B4
B5
T1
T2
T3
T4
T5
BENIGN
TUMOR
N=411 DOWNREGULATED TUMOR PROTEINS
E
REACTOME 2022
Metabolism R-HSA-1430728
Respiratory Electron Transport R-HSA-611105
Citric Acid (TCA) Cycle And Respiratory Electron Transport R-HSA-1428517
Respiratory Electron Transport, ATP Synthesis By Chemiosmotic Coupling, Heat Production By Uncoupling Proteins R-HSA
Complex I Biogenesis R-HSA-6799198
Fatty Acid Metabolism R-HSA-8978868
Mitochondrial Fatty Acid Beta-Oxidation R-HSA-77289
Platelet Activation, Signaling And Aggregation R-HSA-76002
Hemostasis R-HSA-109582
Branched-chain Amino Acid Catabolism R-HSA-70895
F
GO BIOLOGICAL PROCESS 2023
Cellular Respiration (GO:0045333)
Mitochondrial ATP Synthesis Coupled Electron Transport (GO:0042775)
Aerobic Electron Transport Chain (GO:0019646)
Oxidative Phosphorylation (GO:0006119)
Aerobic Respiration (GO:0009060)
Proton Motive Force-Driven Mitochondrial ATP Synthesis (GO:0042776)
Mitochondrial Electron Transport, NADH To Ubiquinone (GO:0006120)
Proton Motive Force-Driven ATP Synthesis (GO:0015986)
Fatty Acid Beta-Oxidation (GO:0006635)
Fatty Acid Catabolic Process (GO:0009062)
G
KEGG ENRICHMENT ANALYSIS
Amyotrophic lateral sclerosis
Chemical carcinogenesis-reactive oxygen species
Huntington disease
Parkinson disease
Prion disease
Thermogenesis
Diabetic cardiomyopathy
Non-alcoholic fatty liver disease
Oxidative Phosphorylation
Propanoate Metabolism
GeneRatio
p.adjust
8.600880e-24
9.294614e-18
1.858922e-17
2.788383e-17
3.717843e-17
Count
20
30
40
50

Figure 4

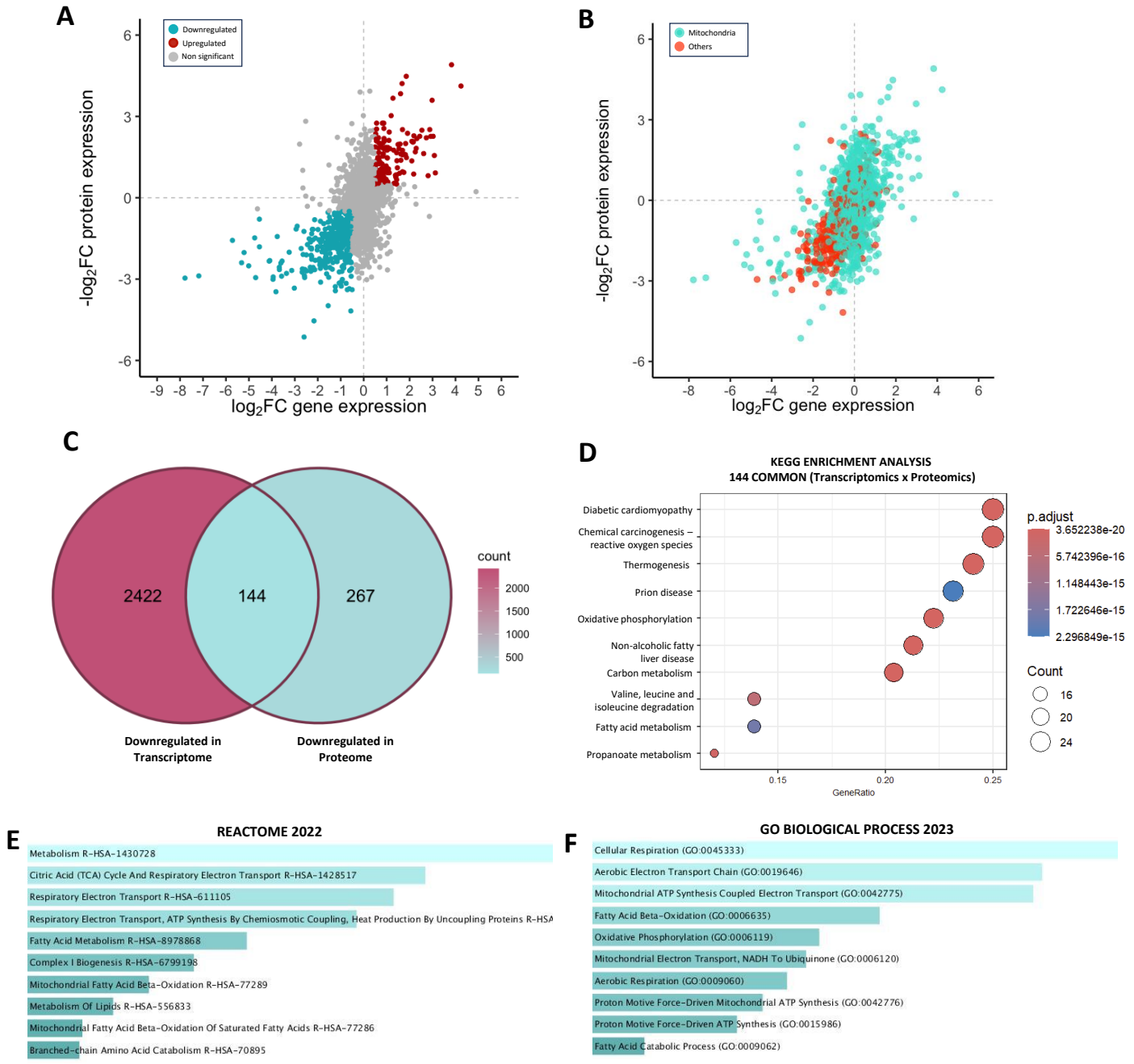
A
Downregulated
Upregulated
Non significant
-log2FC protein expression
log2FC gene expression
B
Mitochondria
Others
-log2FC protein expression
log2FC gene expression
C
2422
144
267
count
2000
1500
1000
500
Downregulated in Transcriptome
Downregulated in Proteome
D
KEGG ENRICHMENT ANALYSIS
144 COMMON (Transcriptomics x Proteomics)
Diabetic cardiomyopathy
Chemical carcinogenesis – reactive oxygen species
Thermogenesis
Prion disease
Oxidative phosphorylation
Non-alcoholic fatty liver disease
Carbon metabolism
Valine, leucine and isoleucine degradation
Fatty acid metabolism
Propanoate metabolism
GeneRatio
p.adjust
3.652238e-20
5.742396e-16
1.148443e-15
1.722646e-15
2.296849e-15
Count
16
20
24
E
REACTOME 2022
Metabolism R-HSA-1430728
Citric Acid (TCA) Cycle And Respiratory Electron Transport R-HSA-1428517
Respiratory Electron Transport R-HSA-611105
Respiratory Electron Transport, ATP Synthesis By Chemiosmotic Coupling, Heat Production By Uncoupling Proteins R-HSA
Fatty Acid Metabolism R-HSA-8978868
Complex I Biogenesis R-HSA-6799198
Mitochondrial Fatty Acid Beta-Oxidation R-HSA-77289
Metabolism Of Lipids R-HSA-556833
Mitochondrial Fatty Acid Beta-Oxidation Of Saturated Fatty Acids R-HSA-77286
Branched-chain Amino Acid Catabolism R-HSA-70895
F
GO BIOLOGICAL PROCESS 2023
Cellular Respiration (GO:0045333)
Aerobic Electron Transport Chain (GO:0019646)
Mitochondrial ATP Synthesis Coupled Electron Transport (GO:0042775)
Fatty Acid Beta-Oxidation (GO:0006635)
Oxidative Phosphorylation (GO:0006119)
Mitochondrial Electron Transport, NADH To Ubiquinone (GO:0006120)
Aerobic Respiration (GO:0009060)
Proton Motive Force-Driven Mitochondrial ATP Synthesis (GO:0042776)
Proton Motive Force-Driven ATP Synthesis (GO:0015986)
Fatty Acid Catabolic Process (GO:0009062)

Figure 5

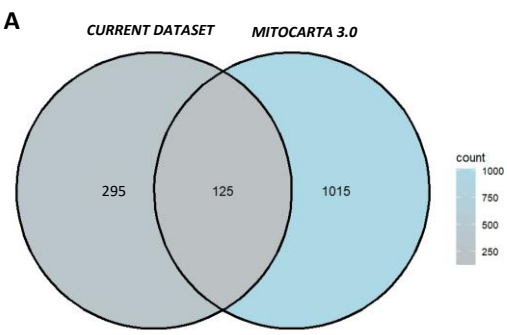
A
CURRENT DATASET
MITOCARTA 3.0
295
125
1015
count
1000
750
500
250

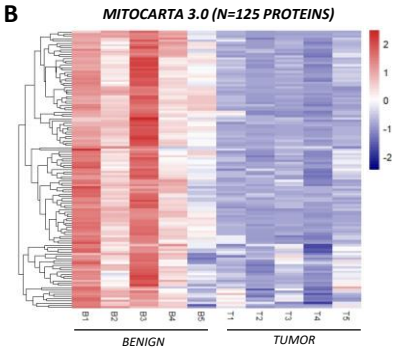
B
MITOCARTA 3.0 (N=125 PROTEINS)
2
1
0
-1
-2
BENIGN
TUMOR

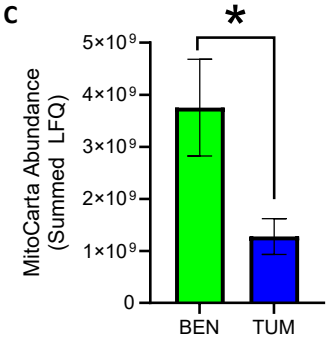
C
*
MitoCarta Abundance (Summed LFQ)
5×10⁹
4×10⁹
3×10⁹
2×10⁹
1×10⁹
0
BEN
TUM

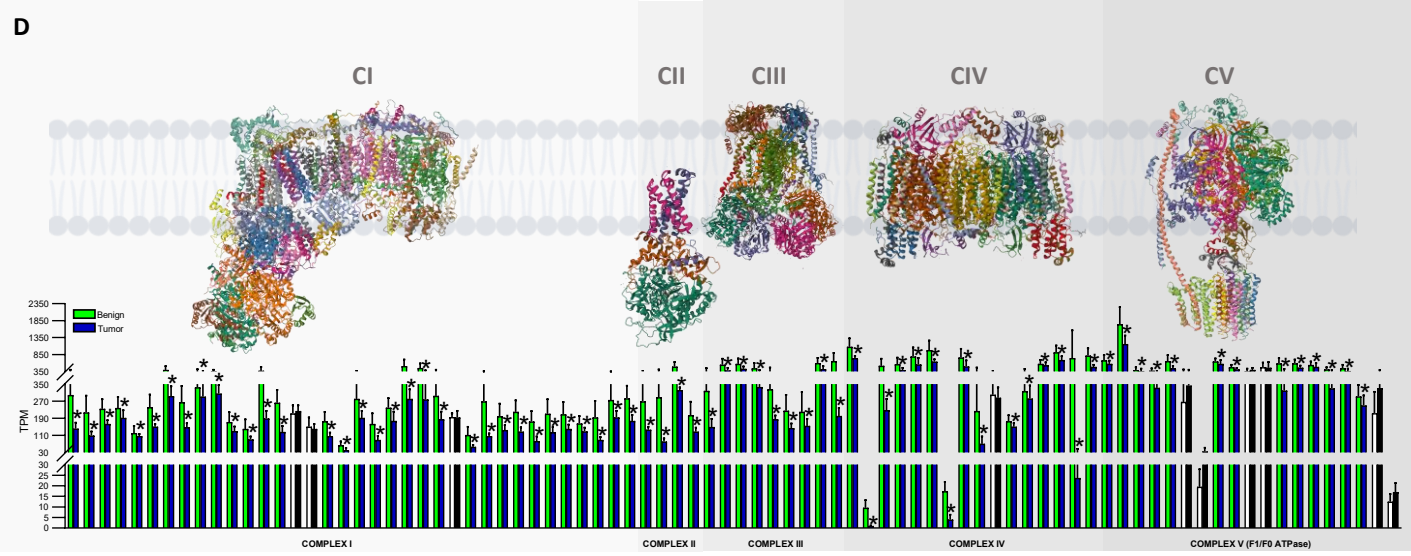
D
CI
CII
CIII
CIV
CV
Benign
Tumor
TPM
COMPLEX I
COMPLEX II
COMPLEX III
COMPLEX IV
COMPLEX V (F1/F0 ATPase)

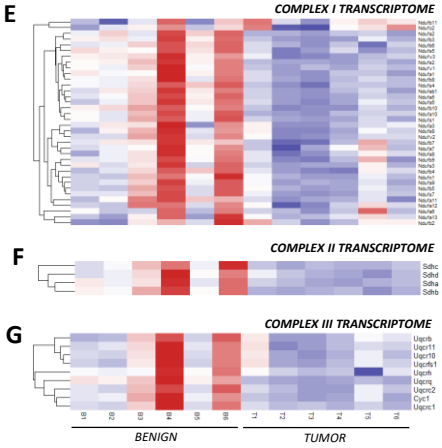
E
COMPLEX I TRANSCRIPTOME
F
COMPLEX II TRANSCRIPTOME
Sdhc
Sdhd
Sdha
Sdhb
G
COMPLEX III TRANSCRIPTOME
Uqcrb
Uqcrf11
Uqcrfs1
Uqcrh
Uqcrq
Uqcrc2
Cyc1
Uqcrc1
BENIGN
TUMOR

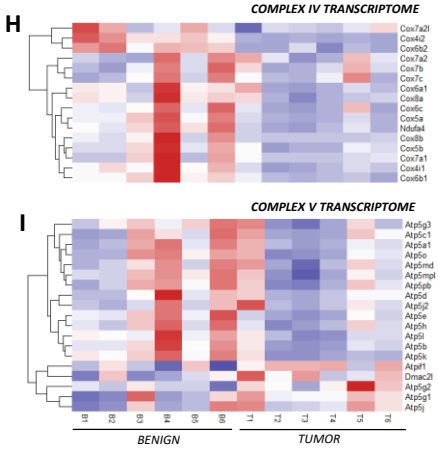
H
COMPLEX IV TRANSCRIPTOME
Cox7a2l
Cox4i2
Cox6b2
Cox7a2
Cox7b
Cox7c
Cox5a1
Cox8a
Cox6c
Cox5a
Ndufa4
Cox8b
Cox5b
Cox7a1
Cox4i1
Cox6b1
I
COMPLEX V TRANSCRIPTOME
Atp5g3
Atp5c1
Atp5a1
Atp5o
Atp5md
Atp5mpl
Atp5pb
Atp5d
Atp5j2
Atp5e
Atp5h
Atp5l
Atp5b
Atp5k
Atpif1
Dmac2l
Atp5g2
Atp5g1
Atp5j
BENIGN
TUMOR

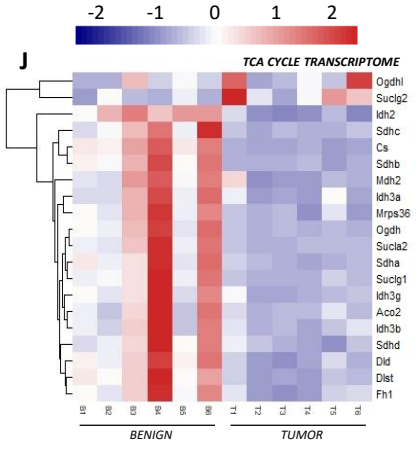
-2
-1
0
1
2
J
TCA CYCLE TRANSCRIPTOME
Ogdhl
Suclg2
Idh2
Sdhc
Cs
Sdhb
Mdh2
Idh3a
Mrps36
Ogdh
Sucla2
Sdha
Suclg1
Idh3g
Aco2
Idh3b
Sdhd
Dld
Dlst
Fh1
BENIGN
TUMOR

Figure 6

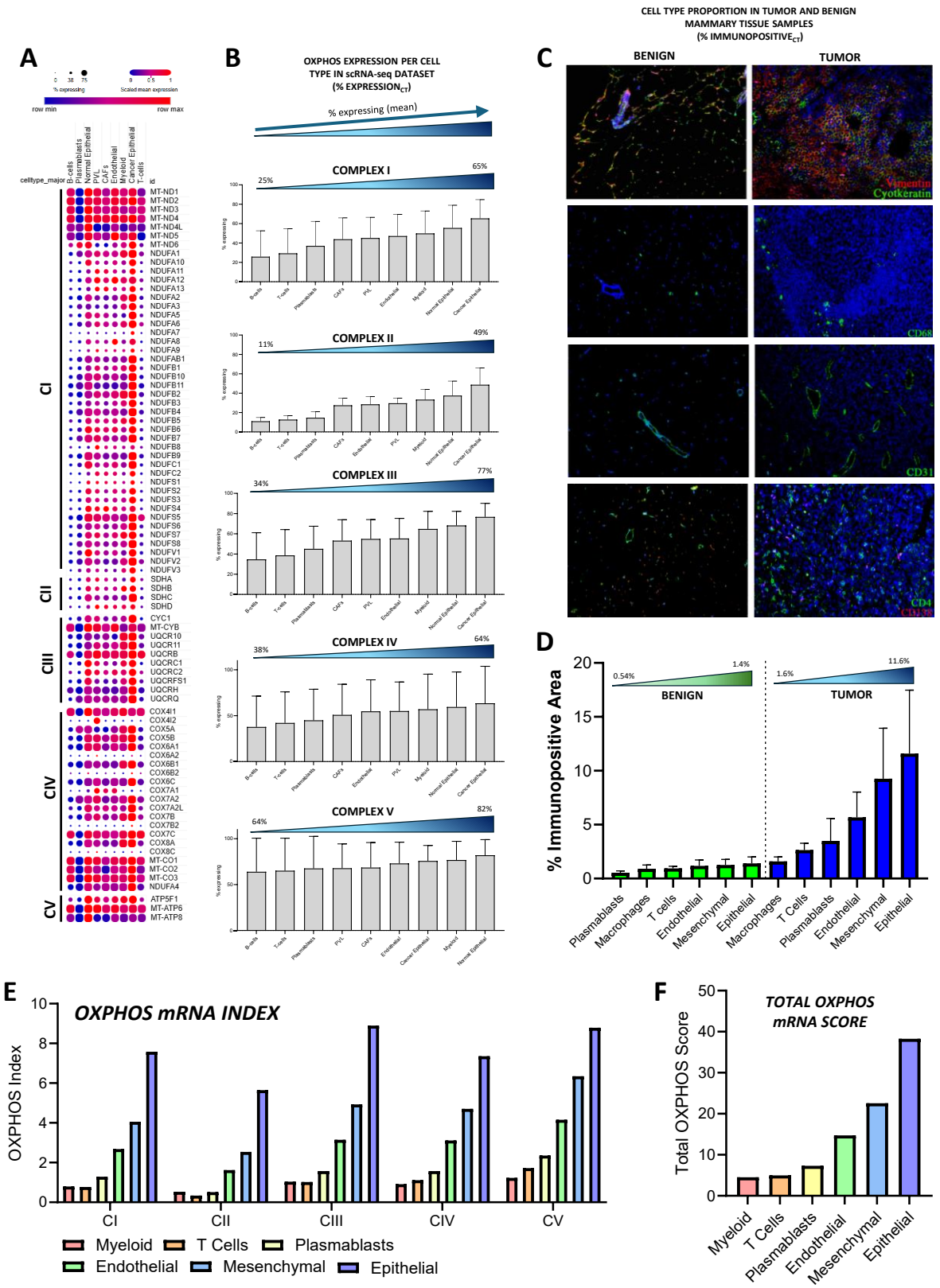
A
% expressing
Scaled mean expression
row min
row max
celltype_major
B-cells
Plasmablasts
Normal Epithelial
PVL
CAFs
Endothelial
Myeloid
Cancer Epithelial
T-cells
id
CI
CII
CIII
CIV
CV
B
OXPHOS EXPRESSION PER CELL TYPE IN scRNA-seq DATASET (% EXPRESSION$_{CT}$)
% expressing (mean)
COMPLEX I
25%
65%
COMPLEX II
11%
49%
COMPLEX III
34%
77%
COMPLEX IV
38%
64%
COMPLEX V
64%
82%
% expressing
C
CELL TYPE PROPORTION IN TUMOR AND BENIGN MAMMARY TISSUE SAMPLES (% IMMUNOPOSITIVE$_{CT}$)
BENIGN
TUMOR
Vimentin
Cytokeratin
CD68
CD31
CD4
CD138
D
% Immunopositive Area
0.54%
1.4%
BENIGN
1.6%
11.6%
TUMOR
Plasmablasts
Macrophages
T cells
Endothelial
Mesenchymal
Epithelial
E
OXPHOS mRNA INDEX
OXPHOS Index
CI
CII
CIII
CIV
CV
Myeloid
T Cells
Plasmablasts
Endothelial
Mesenchymal
Epithelial
F
TOTAL OXPHOS mRNA SCORE
Total OXPHOS Score
Myeloid
T Cells
Plasmablasts
Endothelial
Mesenchymal
Epithelial

Figure 7

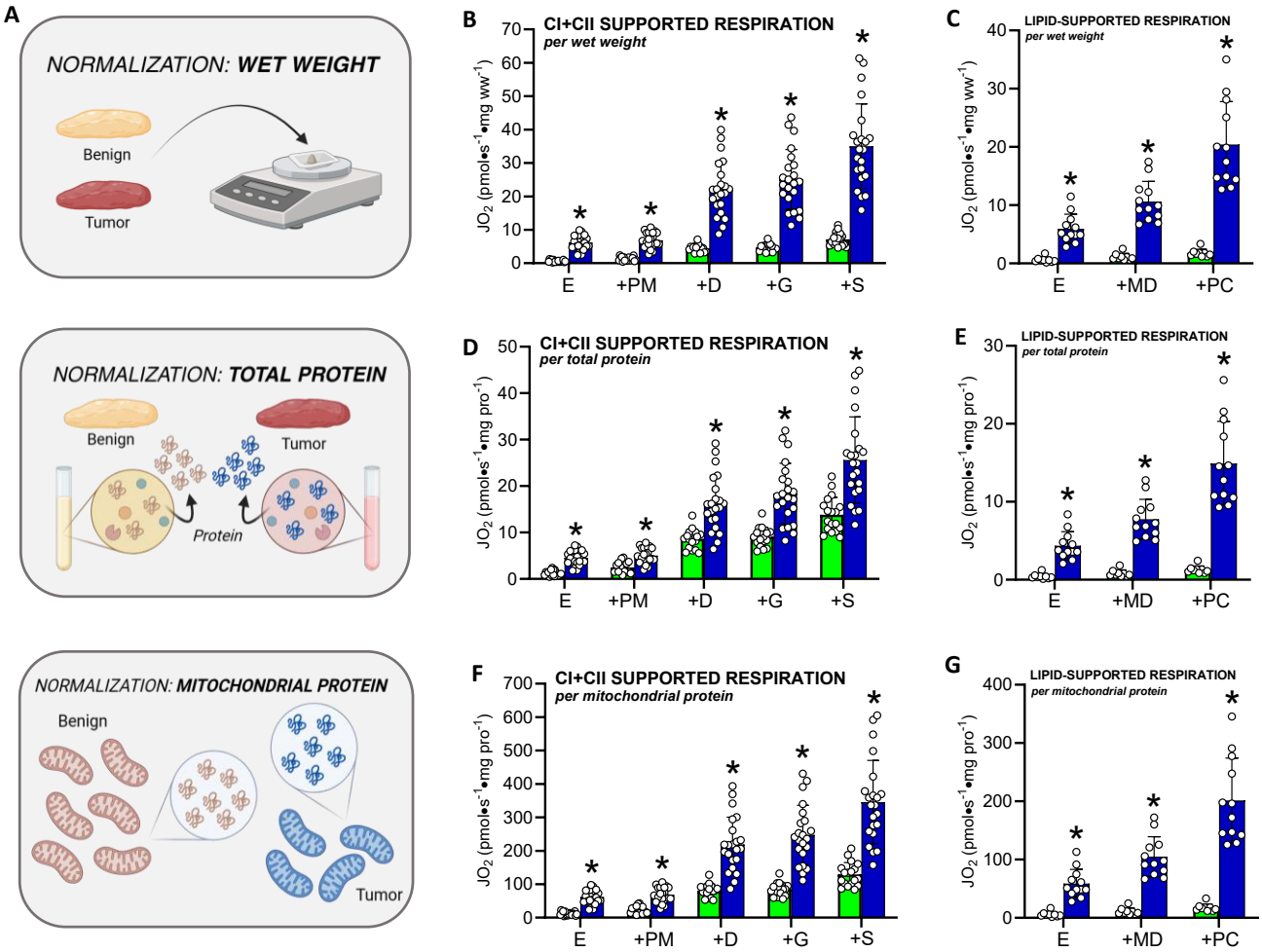
A
NORMALIZATION: WET WEIGHT
Benign
Tumor
NORMALIZATION: TOTAL PROTEIN
Benign
Tumor
Protein
NORMALIZATION: MITOCHONDRIAL PROTEIN
Benign
Tumor
B
CI+CII SUPPORTED RESPIRATION
per wet weight
JO2 (pmol•s-1•mg ww-1)
E
+PM
+D
+G
+S
C
LIPID-SUPPORTED RESPIRATION
per wet weight
JO2 (pmol•s-1•mg ww-1)
E
+MD
+PC
D
CI+CII SUPPORTED RESPIRATION
per total protein
JO2 (pmol•s-1•mg pro-1)
E
+PM
+D
+G
+S
E
LIPID-SUPPORTED RESPIRATION
per total protein
JO2 (pmol•s-1•mg pro-1)
E
+MD
+PC
F
CI+CII SUPPORTED RESPIRATION
per mitochondrial protein
JO2 (pmol•s-1•mg pro-1)
E
+PM
+D
+G
+S
G
LIPID-SUPPORTED RESPIRATION
per mitochondrial protein
JO2 (pmol•s-1•mg pro-1)
E
+MD
+PC

Figure 8

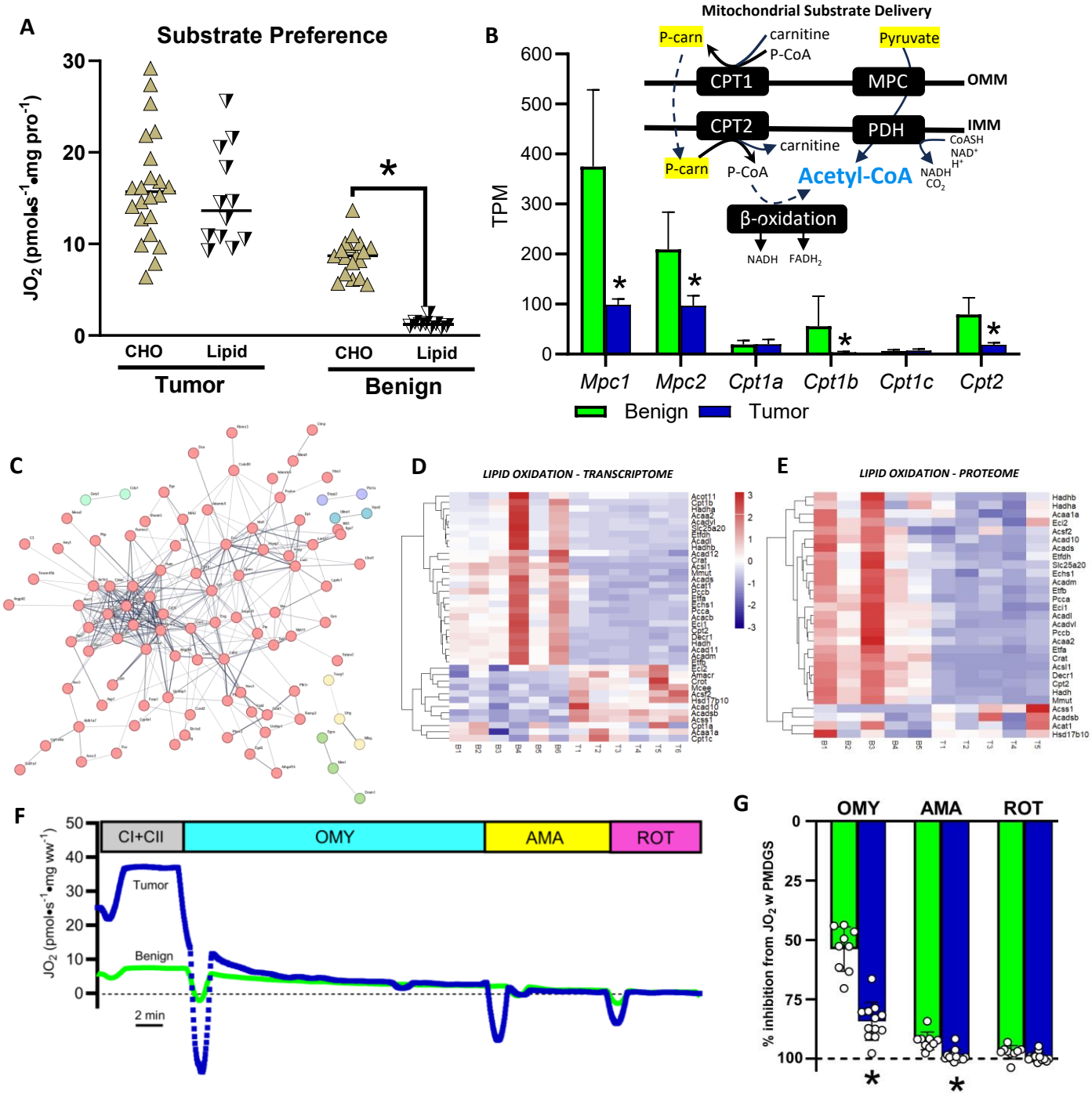
A
Substrate Preference
JO2 (pmol•s-1•mg pro-1)
30
20
10
0
*
CHO
Lipid
CHO
Lipid
Tumor
Benign
B
Mitochondrial Substrate Delivery
P-carn
carnitine
P-CoA
Pyruvate
CPT1
MPC
OMM
CPT2
PDH
IMM
carnitine
P-carn
P-CoA
Acetyl-CoA
CoASH
NAD+
H+
NADH
CO2
β-oxidation
NADH
FADH2
TPM
600
500
400
300
200
100
0
Mpc1
Mpc2
Cpt1a
Cpt1b
Cpt1c
Cpt2
Benign
Tumor
C
D
LIPID OXIDATION - TRANSCRIPTOME
E
LIPID OXIDATION - PROTEOME
F
CI+CII
OMY
AMA
ROT
JO2 (pmol•s-1•mg ww-1)
Tumor
Benign
2 min
G
OMY
AMA
ROT
% inhibition from JO2 w PMDGS
0
25
50
75
100
*
*

Figure 9

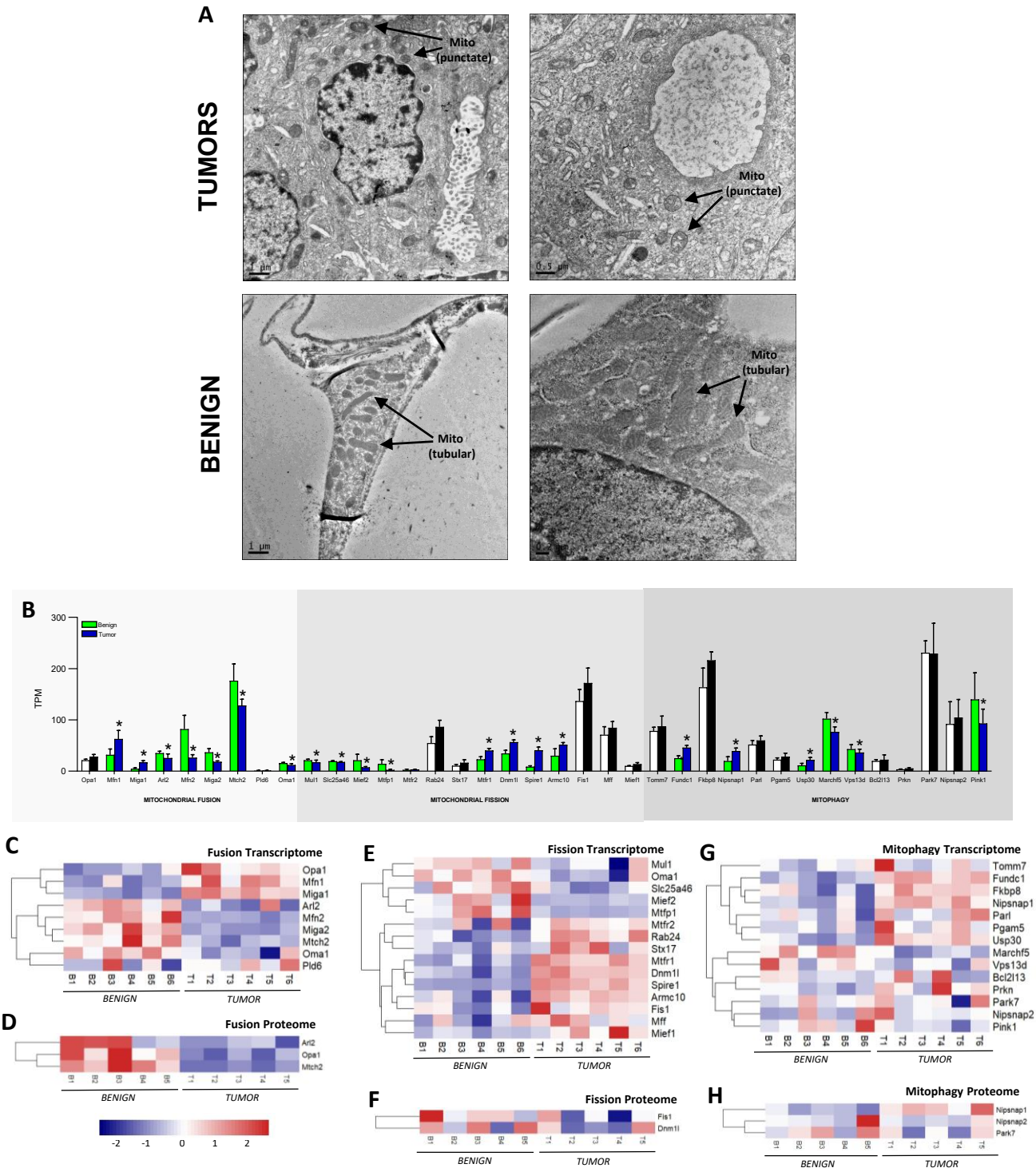
A
TUMORS
BENIGN
Mito (punctate)
Mito (punctate)
Mito (tubular)
Mito (tubular)
1 µm
0.5 µm
B
Benign
Tumor
TPM
300
200
100
0
Opa1 Mfn1 Miga1 Arl2 Mfn2 Miga2 Mtch2 Pld6 Oma1
MITOCHONDRIAL FUSION
Mul1 Slc25a46 Mief2 Mtfp1 Mtfr2 Rab24 Stx17 Mtfr1 Dnm1l Spire1 Armc10 Fis1 Mff Mief1
MITOCHONDRIAL FISSION
Tomm7 Fundc1 Fkbp8 Nipsnap1 Parl Pgam5 Usp30 Marchf5 Vps13d Bcl2l13 Prkn Park7 Nipsnap2 Pink1
MITOPHAGY
C
Fusion Transcriptome
Opa1
Mfn1
Miga1
Arl2
Mfn2
Miga2
Mtch2
Oma1
Pld6
B1 B2 B3 B4 B5 B6 T1 T2 T3 T4 T5 T6
BENIGN
TUMOR
D
Fusion Proteome
Arl2
Opa1
Mtch2
BENIGN
TUMOR
-2 -1 0 1 2
E
Fission Transcriptome
Mul1
Oma1
Slc25a46
Mief2
Mtfp1
Mtfr2
Rab24
Stx17
Mtfr1
Dnm1l
Spire1
Armc10
Fis1
Mff
Mief1
BENIGN
TUMOR
F
Fission Proteome
Fis1
Dnm1l
BENIGN
TUMOR
G
Mitophagy Transcriptome
Tomm7
Fundc1
Fkbp8
Nipsnap1
Parl
Pgam5
Usp30
Marchf5
Vps13d
Bcl2l13
Prkn
Park7
Nipsnap2
Pink1
BENIGN
TUMOR
H
Mitophagy Proteome
Nipsnap1
Nipsnap2
Park7
BENIGN
TUMOR

Figure 10

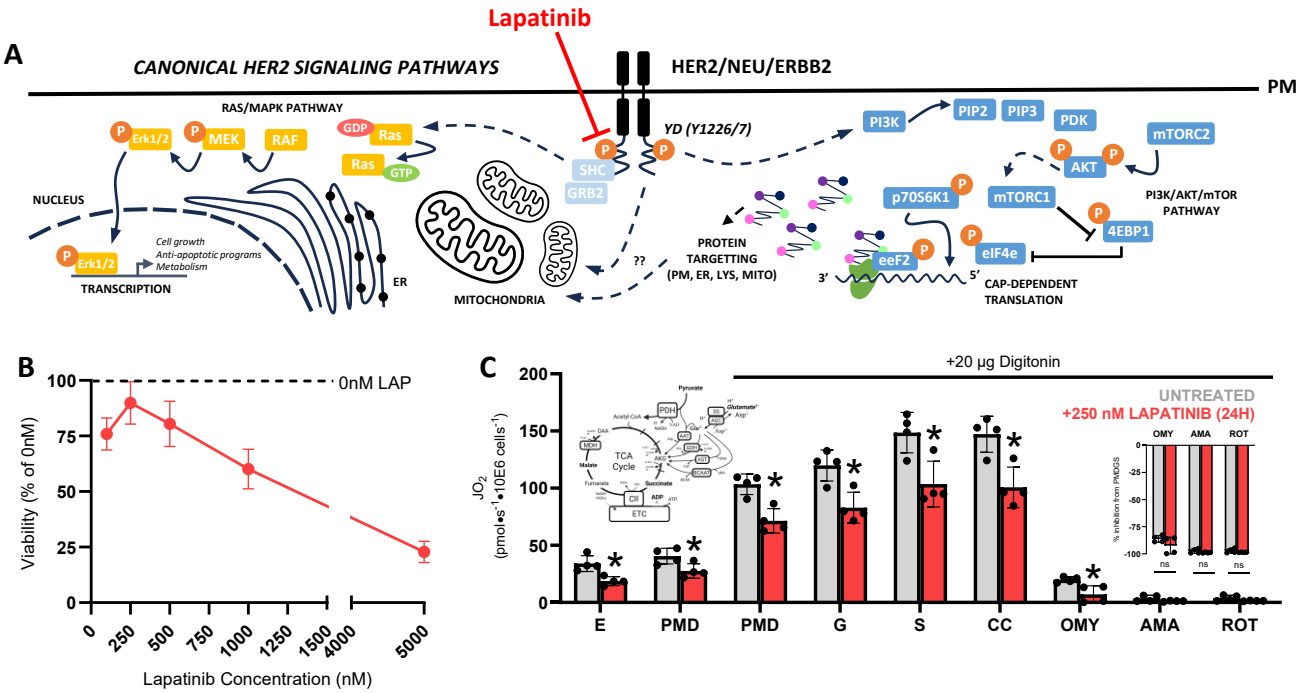
A
Lapatinib
CANONICAL HER2 SIGNALING PATHWAYS
HER2/NEU/ERBB2
PM
RAS/MAPK PATHWAY
Erk1/2
MEK
RAF
GDP
Ras
GTP
YD (Y1226/7)
SHC
GRB2
PI3K
PIP2
PIP3
PDK
mTORC2
AKT
NUCLEUS
Cell growth
Anti-apoptotic programs
Metabolism
TRANSCRIPTION
ER
MITOCHONDRIA
??
PROTEIN TARGETTING (PM, ER, LYS, MITO)
p70S6K1
mTORC1
4EBP1
eIF4e
eeF2
3'
5'
CAP-DEPENDENT TRANSLATION
PI3K/AKT/mTOR PATHWAY
B
0nM LAP
Viability (% of 0nM)
Lapatinib Concentration (nM)
C
+20 µg Digitonin
UNTREATED
+250 nM LAPATINIB (24H)
JO2 (pmol•s-1•10E6 cells-1)
TCA Cycle
ETC
E
PMD
PMD
G
S
CC
OMY
AMA
ROT
% inhibition from PMDGS
ns

Supplementary Figure 1

CANONICAL HER2 SIGNALING - PROTEIN

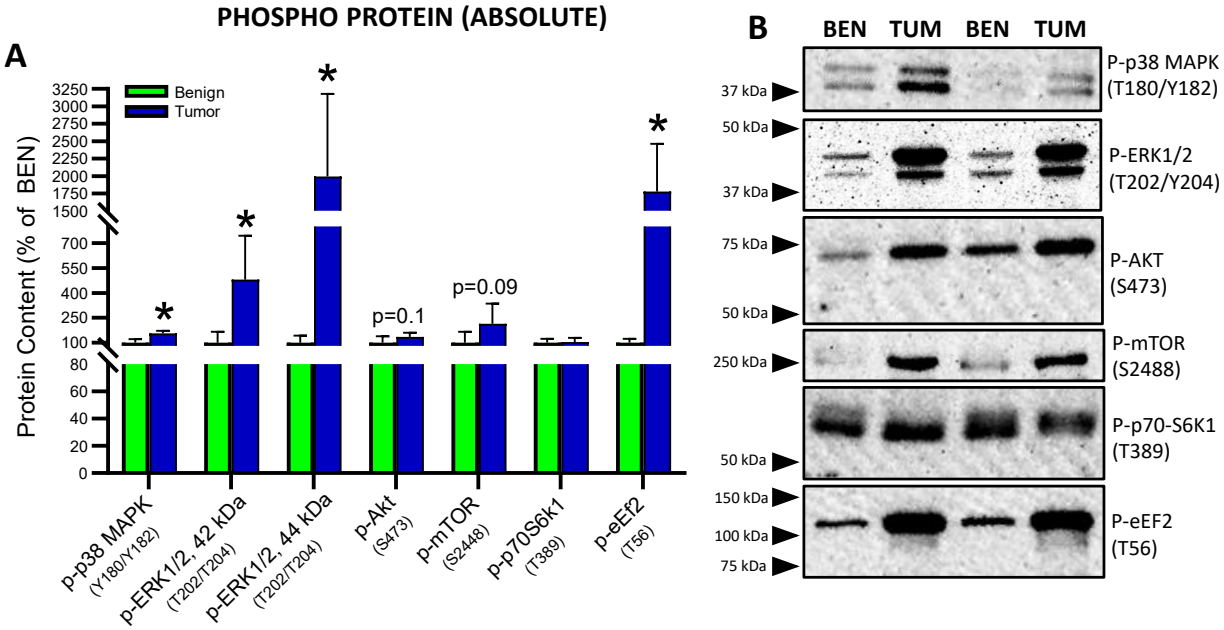

Supplementary Figure 2

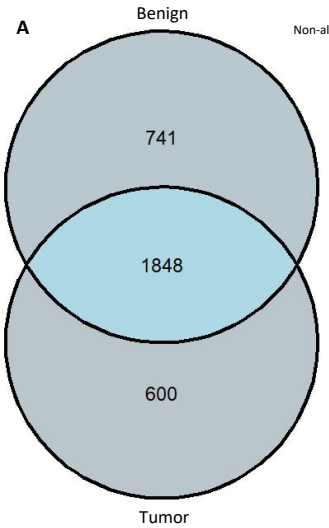

N=741 UNIQUE BENIGN MAMMARY TISSUE PROTEINS

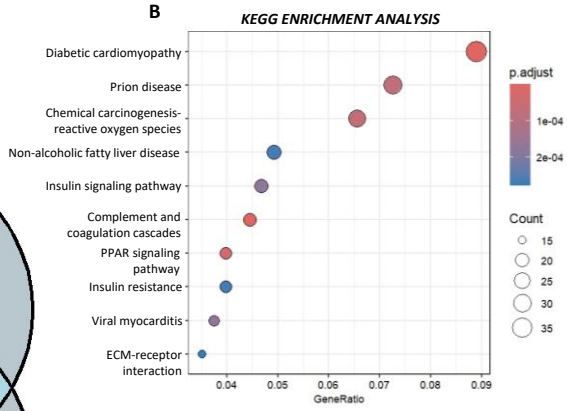

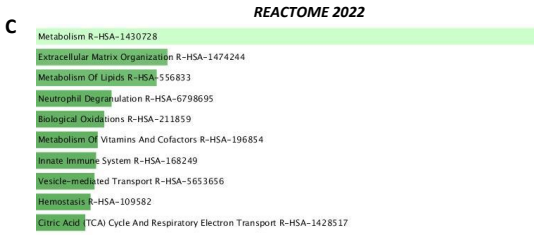

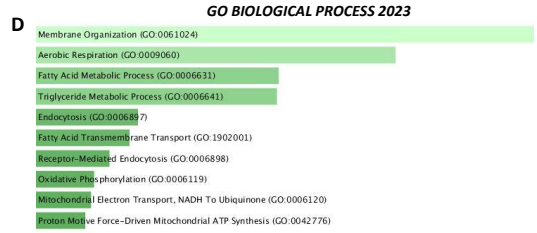

N=600 UNIQUE HER2-DRIVEN TUMOR PROTEINS

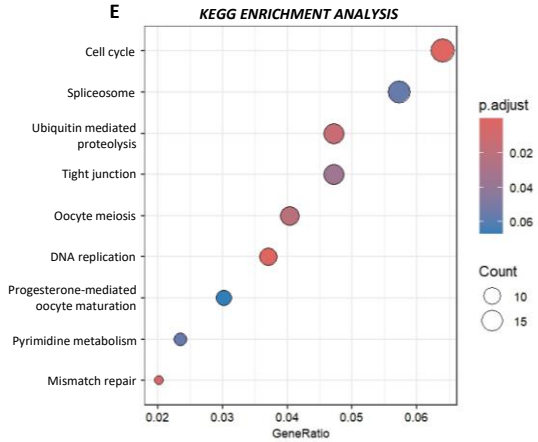

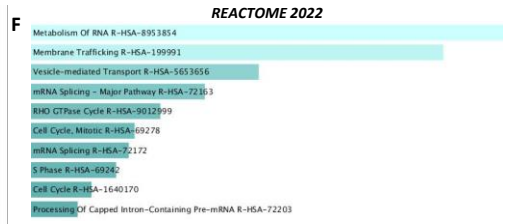

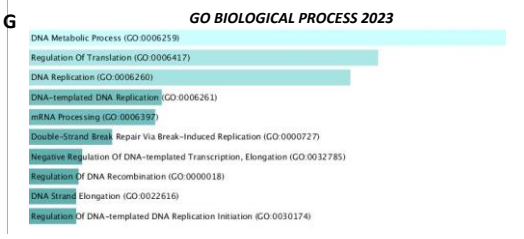

Supplementary Figure 3

$$MEF = \frac{MitoCarta\ Protein\ Abundance}{Total\ Protein\ Abundance}$$

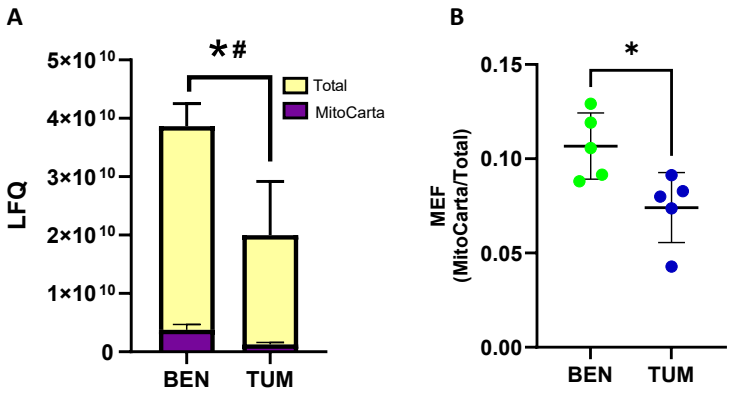

Supplementary Figure 4

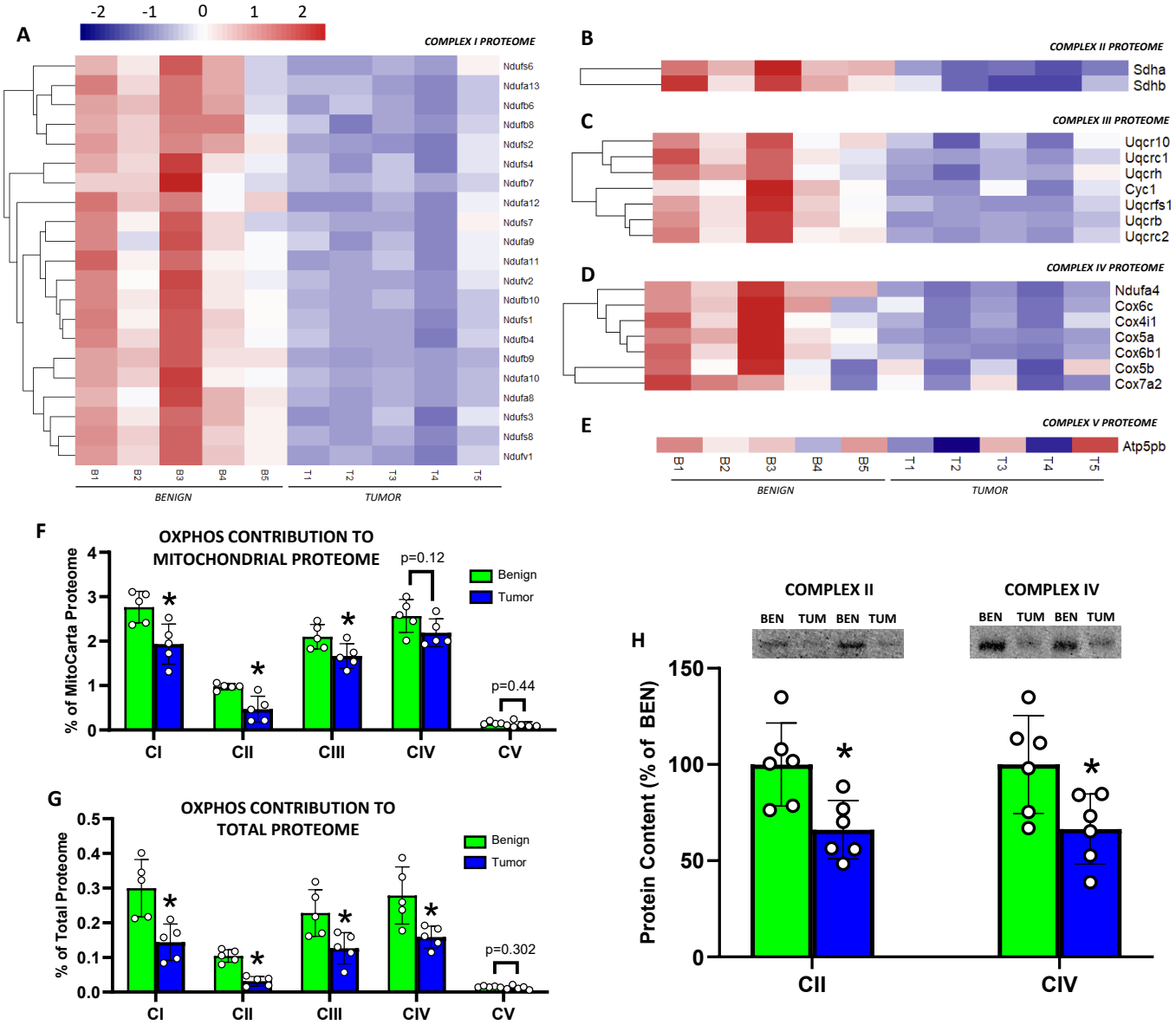

Supplementary Figure 5

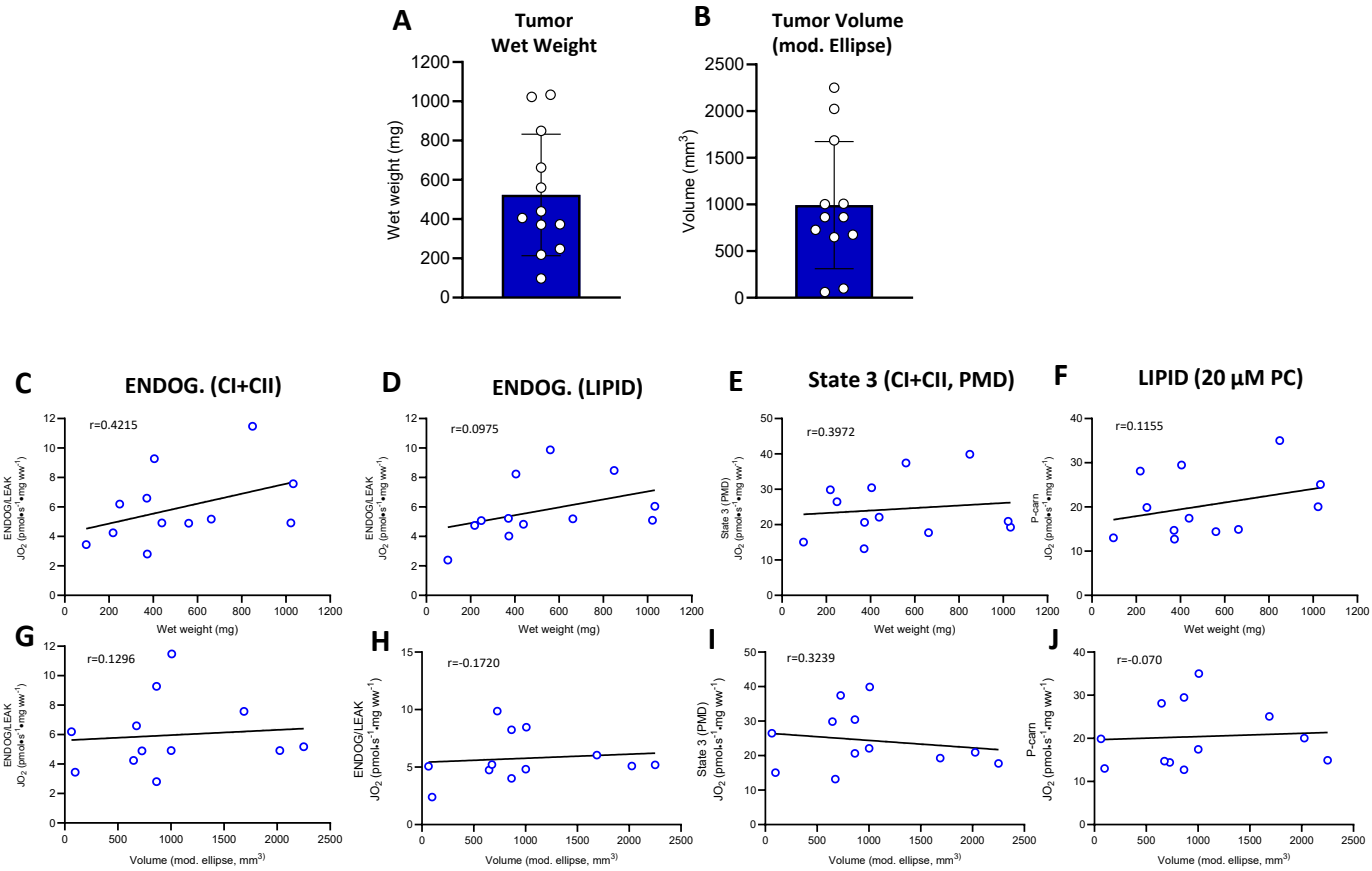

Supplementary Figure 6

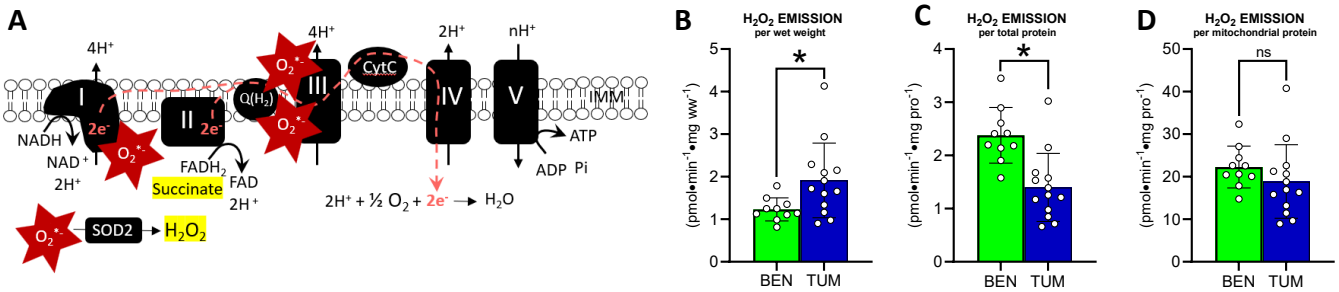

Supplementary Table 1

Abbrev.	Protein	Pathway/Function	Fc (vs BEN)	p.adj
PGK1	Phosphoglycerate kinase	Glycolysis	2.48	0.068
KPYM	Pyruvate kinase	Glycolysis	3.17	0.048
MP2K4	Mitogen activated protein kinase kinase 4	MAPK Pathway	3.65	0.012
RL38	Large ribosomal subunit protein eL38	Protein synthesis/translation	4.11	0.078
PGTA	Geranylgeranyl transferase type-2 subunit alpha	Cysteine prenylation of Rab proteins	4.28	0.067
Rl23	Large ribosomal subunit protein uL14	Protein synthesis/translation	4.41	0.042
CADH1	Cadherin-1	Cell adhesion and motility, epithelial cell marker	12.75	0.084
LMCD1	LIM and cysteine rich domains protein 1	Transcriptional cofactor for GATA6 involved in cell proliferation and metastasis (MMP, EGFR)	15.26	0.077
MPRI	Cation independent mannose 6 phosphate receptor	Lysosomal/Golgi trafficking, associates with IGFR2	22.3	0.093